Journal of Structural Geology 32 (2010) 1806–1826

Contents lists available at ScienceDirect

Journal of Structural Geology

journal homepage: www.elsevier.com/locate/jsg

Structural and petrophysical evolution of extensional fault zones in low-porosity, poorly lithified sandstones of the Barreiras Formation, NE Brazil

F. Balsamo [a,*], F. Storti [a], F. Salvini [a], A.T. Silva [b], C.C. Lima [b]

[a] Università degli Studi Roma Tre, Dipartimento di Scienze Geologiche, 00146 Roma, Italy
[b] Cenpes, Petrobras, Rio de Janeiro, Brazil

ARTICLE INFO

Article history:
Received 5 February 2009
Received in revised form
2 October 2009
Accepted 5 October 2009
Available online 6 November 2009

Keywords:
Grain size reduction
Fractal distribution
Porosity
Cataclasis
Dilatancy
Fault-zone permeability

ABSTRACT

We describe the structural and petrophysical evolution of extensional fault zones developed in low porosity, poorly lithified, quartz-dominated sandstones from the Mio-Pliocene continental Barreiras Formation, NE Brazil. We studied eight fault zones developed as sands were lithified. Fault displacement ranges from a few centimetres to ~50 m. A diagnostic feature of the studied fault zones is the lack of deformation bands, which typically develop in high porosity sand(stone)s. Structural and microstructural analyses, grain size and shape analyses, porosity and pore size analyses, and laboratory and *in situ* permeability measurements show relationships between deformation processes and hydrologic properties. Undeformed rocks are very poorly sorted, medium- to fine-grained, clay-rich sandstones with an average intergranular porosity of about 3%. Sandstones in damage zones record non-destructive dilatant granular flow and formation of opening-mode intergranular extensional fractures, which increase porosity, pore connectivity and permeability. Deformation in fault cores evolved from particulate flow to compactional cataclastic flow, with progressive grain size reduction increasing the amount of silt- and clay-size fractions. Porosity was dramatically reduced to an average value of 0.2% and permeability is generally lower than the related protoliths. All this evidence highlights a conduit/barrier behaviour of the studied fault zones, which significantly differs from the sealing behaviour of deformation band fault zones commonly observed in high-porosity sandstones.

1. Introduction

Porosity and its evolution through time are an important factor controlling what kind of mesoscopic deformation structures develop during rock failure (e.g. Dunn et al., 1973; Vernik et al., 1993; Kwon et al., 2005; Fossen et al., 2007). In the last four decades, considerable attention has been devoted to the understanding of fault zone evolution in high-porosity (>10–15%), lithified to loose granular material both in the field (Aydin, 1978; Aydin and Johnson, 1978; Pittman, 1981; Lucas and Moore, 1986; Antonellini and Aydin, 1994; Fowles and Burley, 1994; Fossen and Hesthammer, 1997; Heynekamp et al., 1999; Cashman and Cashman, 2000; Shipton and Cowie, 2001; Rawling and Goodwin, 2003; Flodin et al., 2003, 2005; Johansen et al., 2005; Minor and Hudson, 2006) and in experimental studies (Borg et al., 1960; Mandl et al., 1977; Menéndez et al., 1996; Wong et al., 1997; Zhu and Wong, 1997; Mair et al., 2000). This because of their important influence on fluid flow in hydrocarbon reservoirs and groundwater aquifers (e.g. Haneberg, 1995; Walsh et al., 1998; Heynekamp et al., 1999; Aydin, 2000; Fisher and Knipe, 2001; Rawling et al., 2001; Manzocchi et al., 2002; Nelson et al., 2009). Deformation in high-porosity granular materials occurs by development of small displacement deformation structures comprehensively referred to as deformation bands, which evolve into zones of deformation bands and slip surfaces with increasing offset (e.g. Aydin and Johnson, 1978; Fowles and Burley, 1994; Shipton and Cowie, 2001; Fossen et al., 2007). A typical result of deformation band faulting in high-porosity sandstones is that their extensive development in fault damage zones may reduce fault transmissibility, thus providing an effective barrier to fluid flow (e.g. Antonellini et al., 1994, 1999; Sigda et al., 1999; Rotevatn et al., 2007). This hydraulic behaviour differs from the typical conduit behaviour of fault damage zones in low-porosity fully lithified rocks, where deformation is dominated by opening-mode fracturing (e.g. Caine et al., 1996; Billi et al., 2003; Kim et al., 2004).

The lower threshold porosity limit for deformation band development is at about 10–15% (e.g. Dunn et al., 1973; Flodin et al., 2003; Wong et al., 1997). Below this threshold limit, shear strength

* Corresponding author. Tel.: +39 0657338049; fax: +39 0657338201.
E-mail address: balsamo@uniroma3.it (F. Balsamo).

0191-8141/$ – see front matter © 2009 Elsevier Ltd. All rights reserved.
doi:10.1016/j.jsg.2009.10.010

becomes a fundamental parameter controlling deformation mechanisms. Joints and slip surfaces are expected to develop in fully lithified sandstones (e.g. Johansen et al., 2005; Fossen et al., 2007). On the other hand, deformation in low-porosity poorly lithified sand(stone)s is still poorly understood. In this paper, we attempt to bridge the gap by describing the structural and petrophysical evolution of extensional fault zones developed in low-porosity, poorly lithified quartz-dominated sandstones of the Barreiras Formation, NE Brazil. The relative compositional maturity and homogeneity of the Barreiras sandstones allow us to discount the effects of clay smearing and tectonic mixing of strongly different sedimentary units within fault zones (e.g. Antonellini and Aydin, 1994; Gibson, 1998; Heynekamp et al., 1999; Caine and Minor, 2009). Results of structural, microstructural, grain size, grain shape, and porosity analyses and permeability measurements are described with the aim of (1) inferring the deformation mechanisms that governed the evolution of these extensional fault zones; (2) proposing an evolutionary model of grain size, grain shape and porosity changes during extensional faulting; and (3) assessing the influence of faulting on fluid flow by establishing a relationship between fault-related permeability variations and fault displacement. The latter provides a useful tool for predicting the expected permeability and transmissibility of sub-seismic and seismic fault zones in sand-dominated clastic reservoirs.

2. Analytical methods

Structural analysis was used to constrain the mesoscale architecture and kinematics of the studied extensional fault zones. Where offset markers were available, stratigraphic separations were measured in the field and then converted into true fault displacement values by using fault kinematics (Butler and Bell, 1989). Fault core thicknesses were measured to determine whether or not there was a predictive statistical relationship that could be used for estimating fault displacement from fault core width when direct measurements were not possible (e.g. Walsh and Watterson, 1988).

Undeformed sandstones and rocks in damage zones and fault cores were sampled at each studied field site. About 0.5 kg of material was collected for each sample. After complete disaggregation and chemical removal of Fe-oxides in the laboratory, grain size analysis of about 60 g of granular material was completed by combining standard sieve and laser diffraction analyses in order to account for coarser (gravel- and sand-size) and finer (silt- and clay-size) fractions, respectively (Selley, 2000). A total of 44 samples were analysed including 17 undeformed sandstones, 16 fault core rocks, and 11 damage zone sandstones. Results of grain size data were plotted as frequency distribution curves using the Phi scale arrangement (Krumbein, 1934, 1938). Grain size distributions were quantitatively described in terms of the following statistical parameters: (a) the mean size Phi_m (a measure of the average size of the curve); (b) the standard deviation So (a measure of the size spread around the mean value, or sorting); (c) the skewness Sk (a measure of the curve symmetry around the mean value, or preferential spread to one side of the mean); and (d) the kurtosis (the degree of concentration of the grain sizes relative to the mean value) (Inman, 1952; Griffiths, 1952). These parameters were obtained by mathematical methods (Folk and Ward, 1957; Krumbein and Pettijohn, 1938) employing the entire sample grain size populations (McManus, 1988). Grain size distributions were also transformed into equivalent particle numbers (e.g. Storti et al., 2003) assuming spherical particles with a density of 2.65 g/cm^3 and plotted against the equivalent size classes in bilogarithmic diagrams to obtain their fractal dimensions (D) as the slope of the best-fit lines (e.g. Blenkinsop, 1991).

Additional non-destructive sampling was carried out in the three structural domains (undeformed sands, damage zones and fault cores) for blue-dyed epoxying and thin section analysis. Microstructural analyses were carried out with a standard petrographic microscope connected to a digital photo camera. Computer-based image analysis techniques (e.g. Francus, 1998; Heilbronner and Keulen, 2006) were applied to thin section images using the Optimas-6.5® commercial software (e.g. Shipton and Cowie, 2001). Colour TIFF images (2568 × 1938 pixel resolution; 1pixel = 2.6 μm) were acquired at constant 1.25× magnification under plane polarised light, in order to ensure the appropriate visualization of both microporosity and macroporosity (i.e. pores with equivalent diameter lower and greater than 63 μm, respectively; Choquette and Lloyd, 1970). A total of 45 images were analysed to characterise thin section sectors representative of undeformed, damage zone and fault core rock fabrics, respectively. Microfabric heterogeneities were addressed by acquiring multiple images from the same thin section.

Images were smoothed by one cycle of 3 × 3 convolution mask filter to remove the background noise and converted to binary images. To avoid sampling errors, only the objects with a 3 × 3 pixel minimum area (i.e. objects with an equivalent diameter greater than 8.8 μm) were considered (Francus and Pirard, 2004). Quantitative thin section analysis of unaltered granular material included: (a) the total percentage of 2D intergranular porosity, calculated as the ratio between void area and total area of the image × 100; and (b) the size of pores, calculated as equivalent diameters (i.e. diameter of the circular area with the same area of the object) and their size distributions. We assumed that 2D porosity is a reasonable approximation of the 3D porosity (e.g. Johansen et al., 2005). Grain shape data were acquired from the different architectural elements of a characteristic fault zone among the studied ones (i.e. undeformed, damaged and fault core domains). Image analysis was applied to thin sections of 3 × 4 cm samples produced from loose grains from the fault zone domains dispersed into blue epoxy. Five standard sand-size classes were separately analysed for grain shape: 1 mm; 0.5 mm; 0.250 mm; 0.125 mm; and 0.063 mm (i.e. Phi = 0, 1, 2, 3, 4, respectively). Angularity (A = Perimeter^2/Area) of at least 100 grains was measured for any size class to ensure a statistically significant population (Anders and Wiltschko, 1994). A total of 54 images from 15 standard thin sections were analysed. Angularity data were represented as frequency histograms and best-fit polymodal Gaussian distributions were determined (Wise et al., 1985) using the software Daisy 4.1 (Salvini, 2004). For comparison, the obtained angularity values were calibrated with the Krumbein (1941) roundness visual chart. As a reference an angularity value of 17.7 corresponds to the threshold value between sub-rounded and sub-angular particles of Krumbein (1941).

Air and gas permeameters were used to measure the permeabilities of protolith sandstones and fault zone structural domains in the field and laboratory, respectively. Laboratory measurements on oriented samples were performed with a gas-permeameter PDPK-400, which provides reliable results from 10^{-6} to greater than 30 Darcy. *In situ* measurements along fault-perpendicular transects starting and terminating in undeformed domains were performed by a portable Tiny-perm II air minipermeameter, which provides reliable permeability values in the range 10^{-4} up to 10 Darcy. Sampling sites were carefully scraped with a putty knife and gently brushed to remove weathering effects prior to permeability measurements. Permeability data were statistically analysed using best-fit polymodal Gaussian distributions.

3. Geological setting

The northeastern part of the Brazilian coastal plain where the study area is located exposes a Precambrian crystalline basement overlain by Cretaceous basinal rocks (Jandaira carbonates and Açu

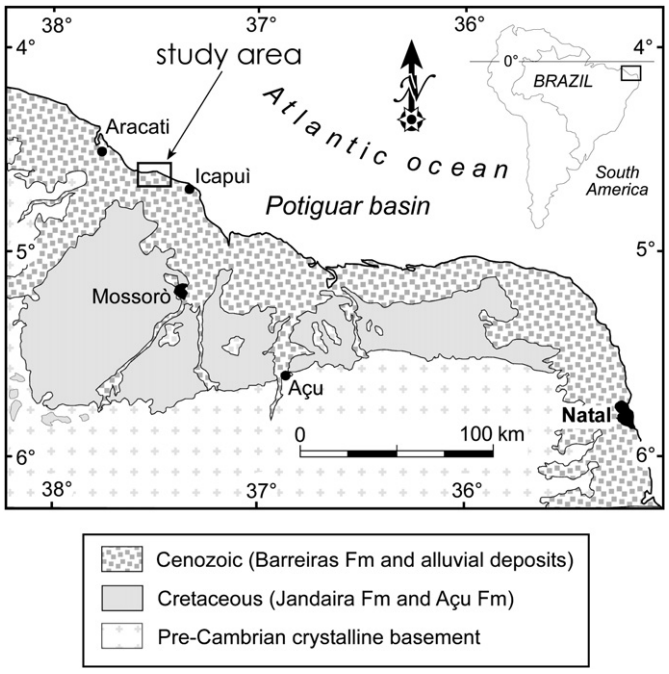

Fig. 1. Simplified geological map of the Potiguar Basin, NE Brazil, showing the location of the study area northwest of the Icapuí village, in the continental Mio-Pliocene Barreiras formation.

fluvial sandstones) and a Cenozoic sedimentary cover (Fig. 1). The latter formed late in the rifting history of the Atlantic ocean and mostly consists of a continental clastic sequence called the Barreiras Formation, which crops out along more than 4000 km of the Brazilian littoral zone from the Amazon delta to the Rio de Janeiro coast (e.g. Mabesoone et al., 1972; Suguio and Nogueira, 1999). The Barreiras formation mainly consists of less-than 100-m thick, poorly lithified, massive quartz-dominated sandstones. The degree of lithification is highly variable and strongly depends on the amount and type of weathering-induced Fe-oxide cementation, which is responsible for the typical orange/yellow to red/violet colours of outcropping sandstones. An early Miocene age of the Barreiras Formation in the study area was obtained by dating detrital and authigenic Fe-pisoliths (using the (U–Th)/He method) from the Barreiras sediments. The age interval is constrained by the minimum age of the detrital pisoliths (22 Ma) and the maximum age of the authigenic pisoliths (17 Ma) (Lima, 2008).

There is clear evidence of post-rift faulting in NE Brazil since the late Tertiary (e.g. Bezerra and Vita-Finzi, 2000). Deformation includes strike-slip and extensional faulting reactivating Precambrian shear zones and generating new structures which controlled sediment deposition and coastal morphology (Bezerra et al., 2001). Significant historical and modern seismicity indicates that faulting is ongoing in the region (Ferreira and Assumpção, 1983; Ferreira et al., 1998).

The study area is located in the western part of the Potiguar sedimentary basin (de Matos, 1992), northwest of Icapuí village, and extends for more than 10 km along the coast (Fig. 1). Cliff exposures mainly consist of Barreiras Formation, although in few

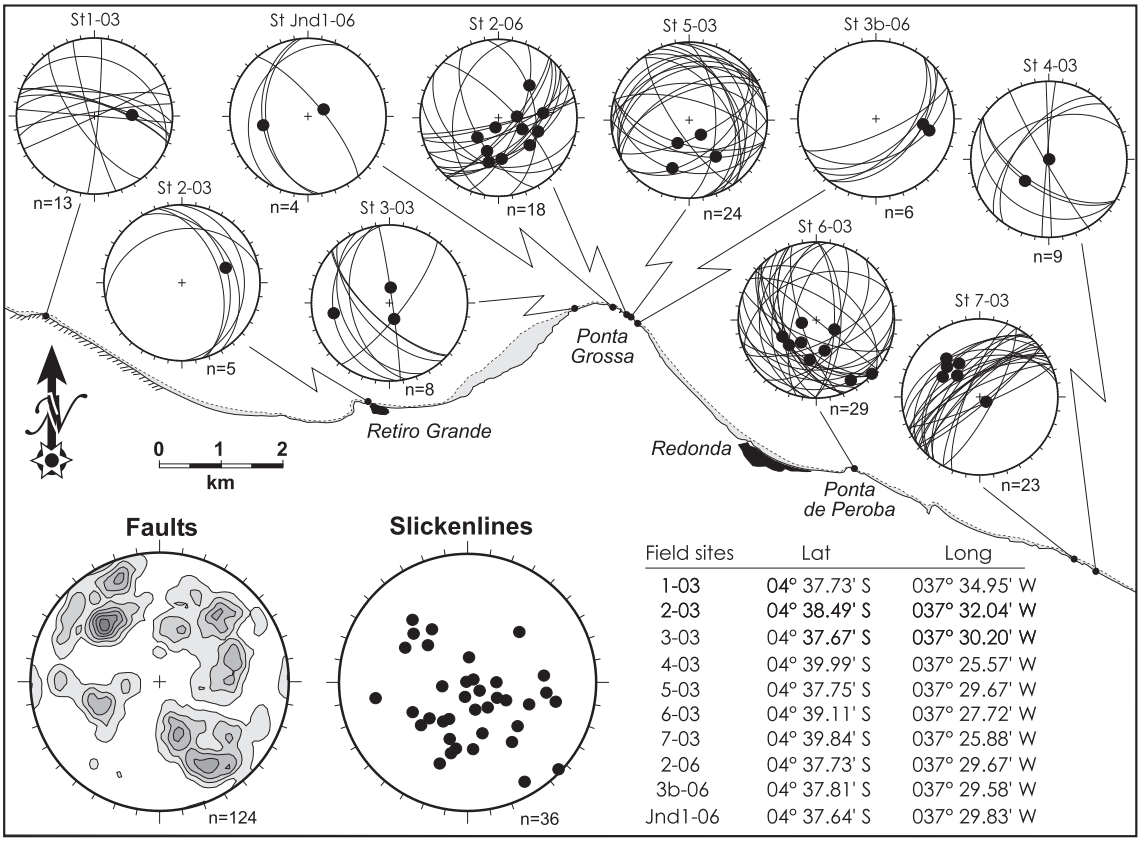

Fig. 2. The studied field sites and lower hemisphere, equal area projections of the measured extensional faults and associated slickenlines. Geographic coordinates are listed. Poles of all measured extensional fault surfaces are contoured at 3% intervals (equal area projection, lower hemisphere). Slickenlines (black dots) are projected in a lower hemisphere, equal area projection. For regional location of the studied area see Fig. 1.

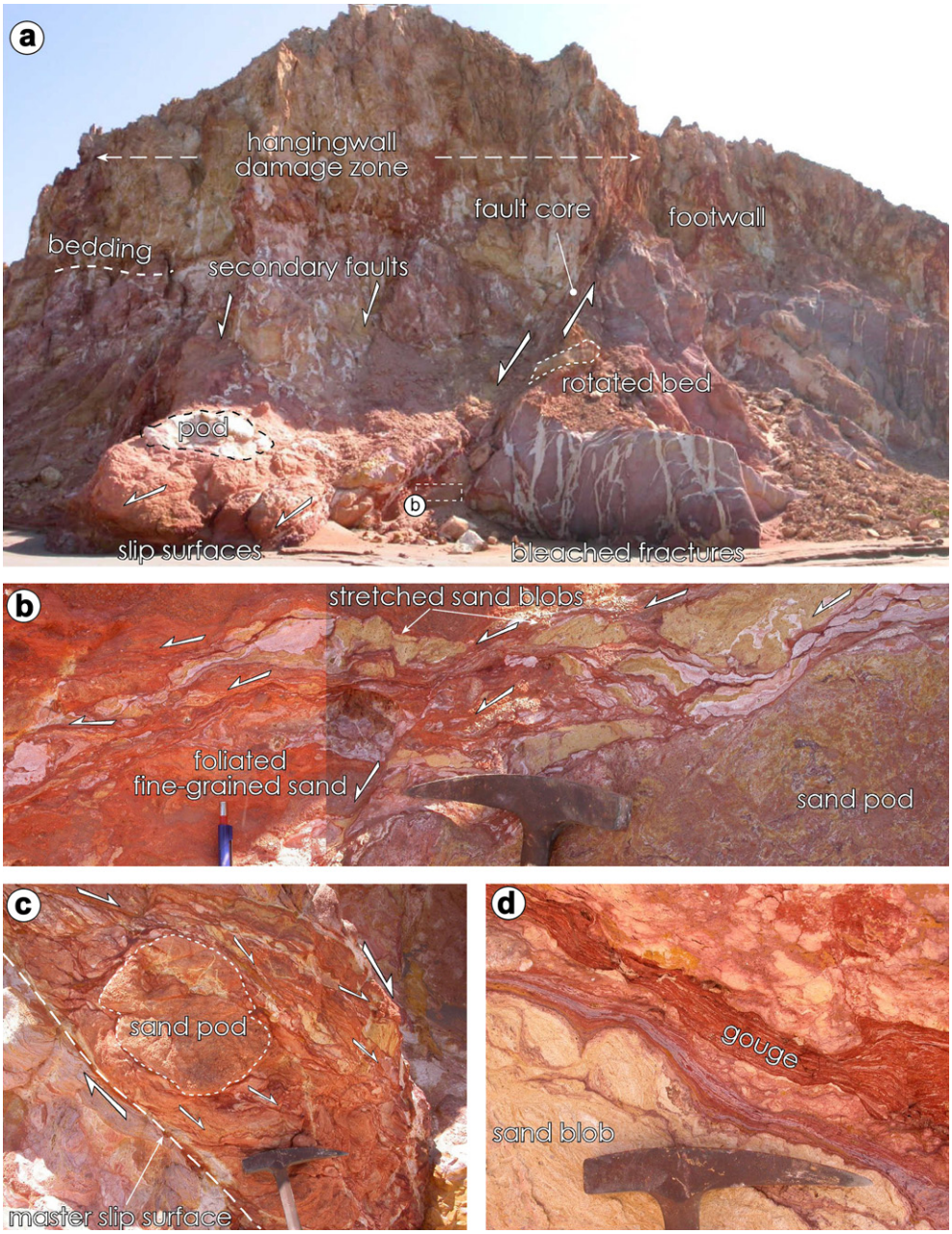

Fig. 3. (a) Structural architecture of an extensional fault zone with about 15 m of displacement consisting of a fault core and hanging-wall and footwall damage zones. The latter is poorly developed and has variable thickness. Subvertical bleached fractures are associated with late stage strike-slip faulting. (b) Detailed view of a typical fault core structural association, including sand pods incorporated during fault movement, foliated clay-rich material, and multiple anastomosing slip surfaces defining an S–C–C′ array. Slip surfaces bound yellow, irregularly stretched, sand 'blobs' which lack original sedimentary fabric. (c) Mesoscopically ductile fabric and pervasive foliation within the fault core, surrounding a weakly deformed, round-shaped sand pod. The fault core-damage zone boundary consists of a striated master slip surface. (d) Stretched and internally foliated yellow sand blob within the fault core, showing cuspate boundaries with strongly foliated fault gouge.

sites the Jandaira carbonates crops out in both stratigraphic and tectonic contact with the overlying Barreiras sandstones.

4. Structural outline

The complex fault pattern exposed in the study area is characterised by abundant fault segments showing different kinematics, orientation, amount of displacement, and deformational styles (Fig. 2). In particular, extensional fault segments have variable orientations, though they exhibit dominant NE and secondary NNW strikes. Cross-cutting relationships indicate that extensional faults are generally overprinted by sub-vertical strike-slip faults. The major extensional fault segments are generally associated with faultward thickening of syn-tectonic sediments in the hanging-walls, pointing to the occurrence of fault activity during the deposition of the Barreiras sandstones. Field observations (described in following sections) indicate that most of the major extensional fault zones developed in soft sediment conditions, while strike-slip faulting occurred in soft up to partially lithified granular material, as indicated by the systematic presence of sub-vertical extensional fractures in damage zones. For this study we carefully selected field sites where structures associated with strike-slip fault zones were negligible or not visible at the outcrop scale.

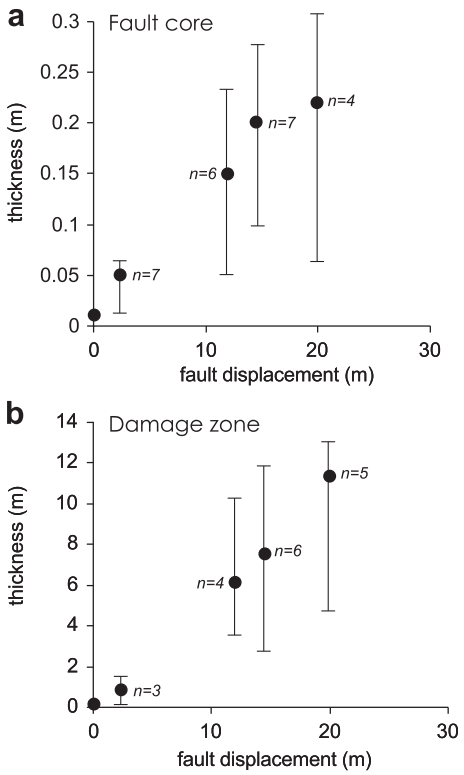

Fig. 4. Fault core (a) and damage zone (b) thickness–displacement relationships measured in the studied fault zones. Error bars represent minimum and maximum values.

4.1. Architectural elements

The internal structure of the studied fault zones (Fig. 3a) consists of three main architectural elements: undeformed protolith, damage zone, and fault core, which accommodated the majority of the slip (e.g. Chester et al., 1993; Caine et al., 1996).

Fault cores exhibit macroscopically distributed ductile structures (cf. Rutter, 1986; Rawling and Goodwin, 2006) without extensive localisation (Fig. 3a–c). Their internal fabric is extremely heterogeneous at the mesoscale due to the occurrence of closely spaced and multiple, anastomosing slip surfaces oriented sub-parallel to the master slip surfaces and forming S–C–C′ structural arrays (e.g. Passchier and Trouw, 1996) (Fig. 3b). Slip surfaces separate strongly foliated red/orange fine-grained sand layers, irregularly stretched yellow sand 'blobs', and sand 'pods' (Fig. 3c and d). Sand pods are 30–80 cm wide and their shape varies from elongate in the direction of fault movement to sub-rounded. Pods have relatively sharp boundaries and locally preserve sedimentary structures. Conversely, yellow sand blobs are 5–20 cm long and are generally strongly elongate. Blobs show irregular globular to cuspate boundaries and their internal sedimentary fabric is partially or completely disrupted. Despite the initial relative homogeneity of the Barreiras Formation, fault core width is locally highly variable along both fault strike and dip within the same fault zone.

Fault cores are typically bound by two master slip surfaces and are generally surrounded by structurally heterogeneous hanging-wall and footwall damage zones. In some cases, however, the latter are partially developed or absent (Fig. 3a). Damage zones typically include widespread mobilised sediments (e.g. Maltman and Bolton, 2003) where sediments are transposed into foliation (Fig. 3a) and partially cemented beds are attenuated, folded, and, eventually, disrupted. These features resemble the mixed zones described by Heynekamp et al. (1999) and Rawling and Goodwin (2003) in high-porosity, poorly lithified sediments. The boundaries between damage zones and the undeformed sandstones are typically gradual and were placed at points where the sub-horizontal undeformed bed attitude started to be reworked by deformation. Zones of deformation bands sub-parallel to the main fault surfaces (e.g. Aydin, 1978; Rawling and Goodwin, 2003) were not recognised neither at the boundary between mobilised sediments and undeformed protoliths, nor adjacent to the master slip surfaces. In some cases, the macroscopically ductile fabrics in the damage zones are overprinted by minor faults and localised dilatant fractures.

In the range of measured displacements (0.1–20 m), mean fault core and damage zone thicknesses in 5 fault zones linearly increase with increasing displacement (Fig. 4). For the construction of diagrams in Fig. 4 we used mean thicknesses of cores and damage zones, obtained by averaging several across-fault measurements. The obtained scaling relationships were then used for calculating fault displacement of fault zones where unambiguous reference markers were not available or where fault displacement exceeded the cliff height.

4.2. Microstructural features

From a textural and mineralogical point of view, undisturbed materials are poorly sorted, grain-supported quartz-dominated sandstones with a wide range in pore size and thin, pore-filling Fe-oxide cement bonds. Coarser grains are sub-angular and elongate showing a slight preferential orientation parallel bedding (Fig. 5a and b).

The most common feature of the studied extensional fault damage zones is the widespread presence of zones where larger clasts are further apart than in the undeformed sand, and are separated by finer grained material (Fig. 5c). Quartz grains show a loose packing geometry and coarser grains do not show any preferential orientation. Locally, poorly foliated sands occur along subsidiary fault splays. Fe-oxide cement is patchily distributed within damage zones. In some locations, localised opening-mode deformation structures such as dilation bands (Du Bernard et al., 2002) and extensional fractures were observed. Extensional fractures developed as irregular intergranular opening-mode fractures with sharp boundaries that mainly follow the coarser grain rims (Fig. 5d). Extensional fractures mainly formed in tighter and/or more cemented granular packages (Fig. 5d–f). Their apertures are generally less than 100 μm. In some cases, intergranular extensional fractures are filled by Fe-oxide cement (Fig. 5e), whereas in other cases they cut cement bonds (Fig. 5f). Dilation bands typically occur at intergranular extensional fracture tips and are characterised by diffused, gradational boundaries with respect to the host sandstone. They have an average thickness of about 0.5–1 mm (Fig. 5g).

Thin section analysis on fault core rocks was performed on foliated clay-rich sands, which generally exhibit variable grain size and porosity. Key observations include: 1) a general decrease in the mean grain size relative to damage zone samples, with coarse elongate and angular survivor grains dispersed in a medium to fine-grained matrix (Fig. 6a); 2) fault-parallel alignment of elongate coarse and fine grains which define the foliation (Fig. 6b); 3) at the grain scale, the coarser quartz grains exhibit distributed intragranular fracturing and flaking (Fig. 6c). In low-displacement faults (<1 m) dilational fabrics in damage zones are separated from tighter packing in fault core rocks by diffuse boundaries (Fig. 6d). Fe-oxide cement in fault core rocks was rarely observed.

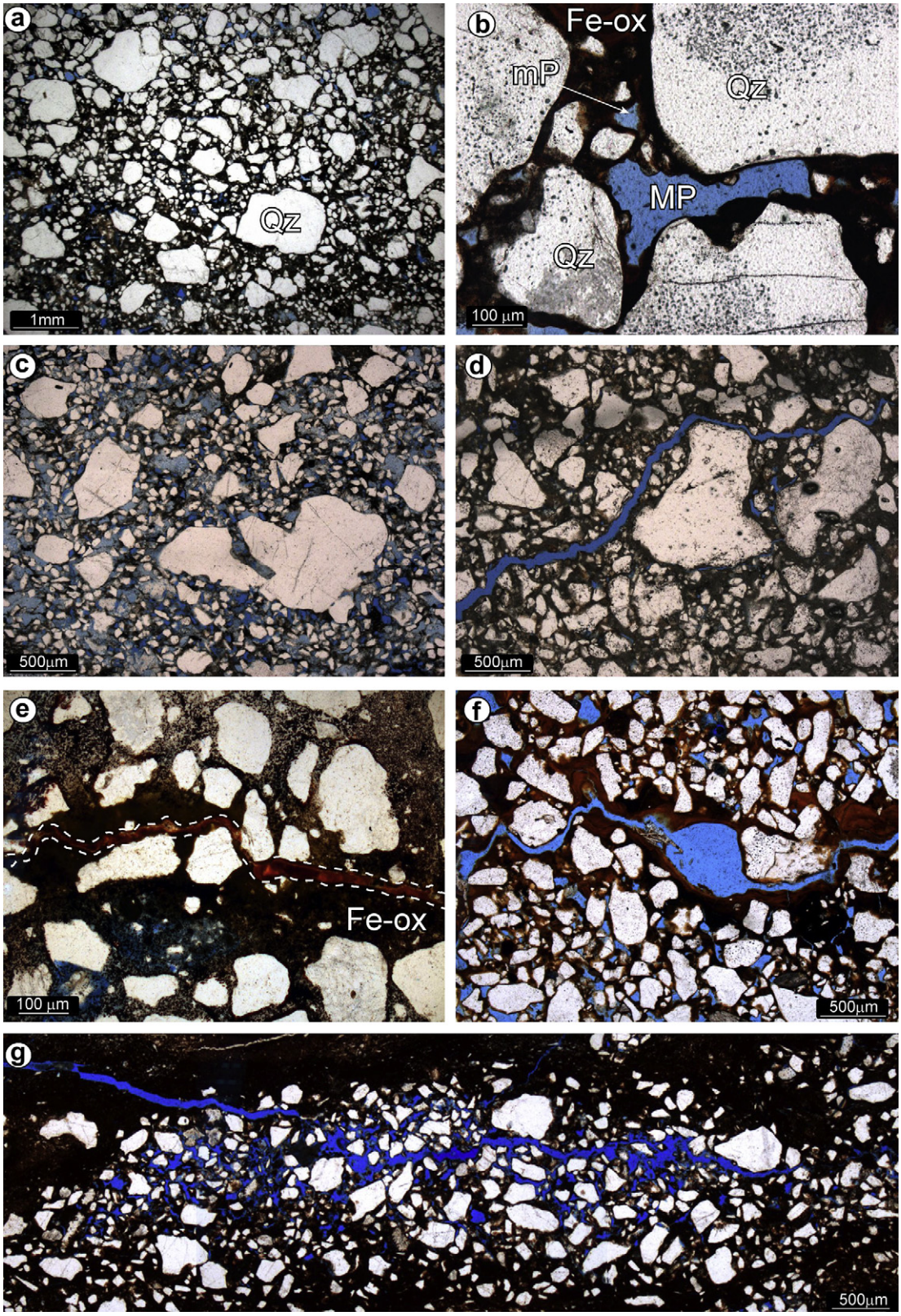

Fig. 5. Plane-polarised-light photomicrographs of undeformed (a, b) and damage zone (c–g) sandstones impregnated with blue epoxy. (a) Undeformed sandstone of the Barreiras formation showing the well cemented, low-porosity and quartz-dominated composition. Quartz sand grains (Qz) are sub-angular to very angular. (b) Example of 2D intergranular primary porosity (in blue) consisting of microporosity (mP) (i.e. pores with equivalent diameters <63 μm), and macroporosity (MP) (i.e. pores with equivalent diameters >63 μm). Quartz grains are bonded by Fe-oxide meniscus cement. (c) Loose packing fabric in the hanging-wall damage zone of a fault zone with displacement of ~20 m. Note sub-angular to very angular quartz grains. (d) Intergranular extensional fracture in the hanging-wall damage zone of a fault zone with estimated displacement of ~35 m. Such structures typically overprint a pre-existing fabric. (e) Fe-oxide-filled intergranular extensional fracture. (f) Intergranular extensional fracture developed in a well cemented sandstone. (g) Dilation band developed in coarse-grained sandstone at the tip of an extensional fracture.

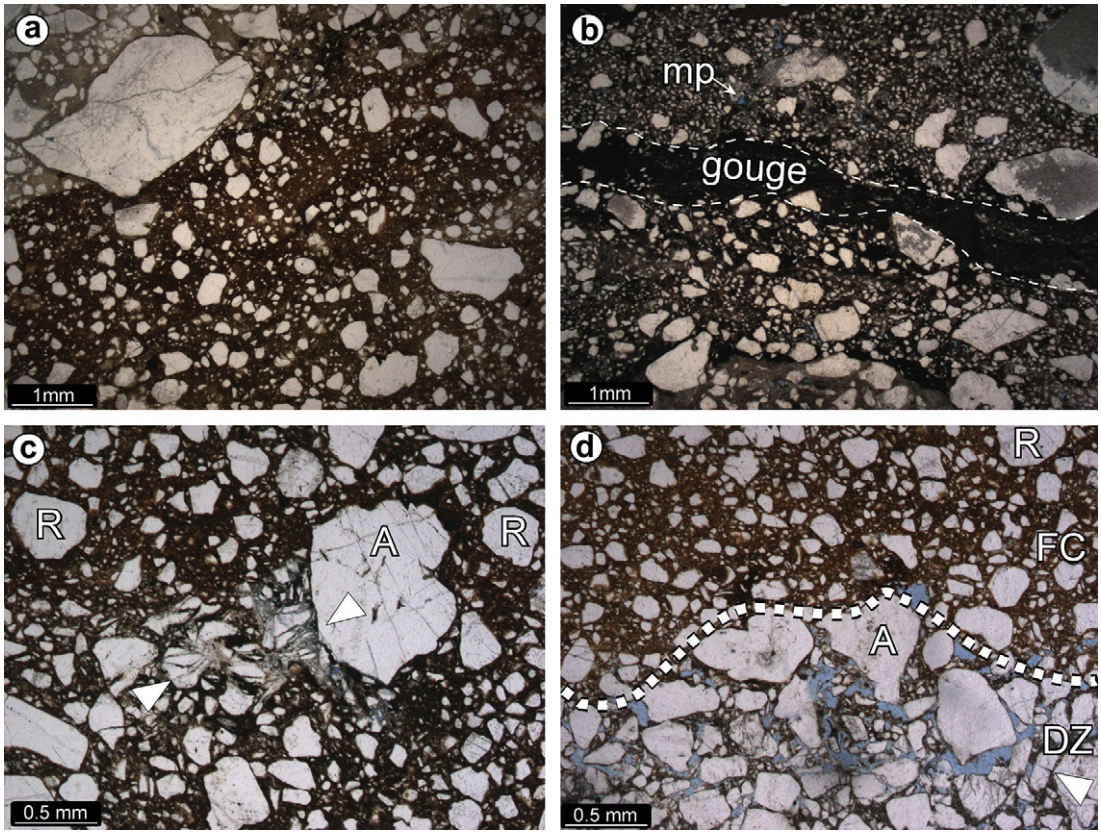

Fig. 6. Plane-polarised-light photomicrograph from fault core samples impregnated with blue epoxy. (a) Tight packing fabric in the fault core of a fault zone with displacement of ~25 m. Coarse, angular, 'survivor' quartz grains are surrounded by a fine-grained matrix. (b) Foliation imparted by the preferential alignment of coarse and fine grains surrounding a narrow gouge seam. Note difference in grain-size distribution above and below the gouge. (c) Example of both rounded (*R*) and angular (*A*) coarse grains surrounded by very angular and elongated finer fragments produced by intense crushing of the coarser grains (arrows). (d) Boundary (dotted line) between very low-porosity fault core (FC) and relatively high-porosity damage zone (DZ) in a fault zone with displacement < 3 m. *A* = angular grain, *R* = rounded grain.

5. Undeformed sandstone characterisation

5.1. Grain size analysis

Results of grain size analyses on 17 samples of undeformed sandstone collected at different field sites are summarised as frequency curves (weight %) in Fig. 7a, while sedimentological statistical parameters are listed in Table A1 (see Appendix). The percentage of gravel-size material (>2 mm) ranges from 0.1% to 7.7% with an average value of 1.76 ± 2.53%. The sand-size fractions (2–0.063 mm) are the most abundant ones and vary from 42.63% up to 82.75%, with an average value of 66.2 ± 6.39%. The silt-size fractions (0.063–0.004 mm) ranges from 10.22% to 21.63%, with an average value of 11.8 ± 2.95%. The cumulative residual clay-size fractions (<4 μm) ranges from 5.67% (clean sandstone) up to 35.68% (impure or clay-rich sandstone) with an average value of 23.2 ± 2.6%.

The mean size (Phi_m) varies from 2.34 (fine sand) to 5.22 (medium silt) with an average value of 3.4 ± 0.66 (very fine sand). The most representative size classes (i.e. the modes) of the undeformed samples are Phi = 2 (medium sand, grain diameter between 0.5 and 0.25 mm) and Phi = 3 (fine sand; 0.25–0.125 mm). Sample sorting varies between 2.25 and 3.62 with a mean value of 3 ± 0.32 (very poorly sorted). Skewness ranges from −0.19 (near symmetrical granulometric curve) up to 1.35 (very fine-skewed curve), with a mean value of 0.6 ± 0.3 (slightly coarse skewed). Kurtosis varies between 1.43 (very platykurtic curve) and 4.21 (leptokurtic curve); the average value is 1.6 ± 0.16 (platykurtic curves). The fractal dimension of the undeformed samples is quite homogeneous varying from 2.42 up to 3.06 with an average value of 2.7 ± 0.11.

5.2. Porosity and permeability

Five thin sections from five undisturbed samples were selected to quantify the intergranular porosity and the corresponding pore size distributions. A total of 17 digital images were analysed. In all the analysed thin sections, pore size mainly varies from 32 to 125 μm (Fig. 8a). Measured intergranular porosity ranges between 1.66 ± 0.5% and 6.77 ± 0.14% (Fig. 8b); thus, these are low porosity, generally moderately cemented sandstones. The contribution of micro and macroporosity is almost equivalent.

Permeability in the undeformed sandstones was measured at six field sites. Permeability statistics are summarised in Fig. 8c. Measured permeability ranges from 0.63 to 233.69 md, with mean values spanning two orders of magnitude from 2.61 ± 0.35 to 70.35 ± 0.26 md.

6. Damage zone characterisation

6.1. Grain size analysis

Grain size analyses were performed on samples collected both in the hanging-wall and footwall damage zones of five extensional faults with different displacement values. Grain size distributions are more variable than those of undeformed samples since they underwent different amounts and types of deformation during

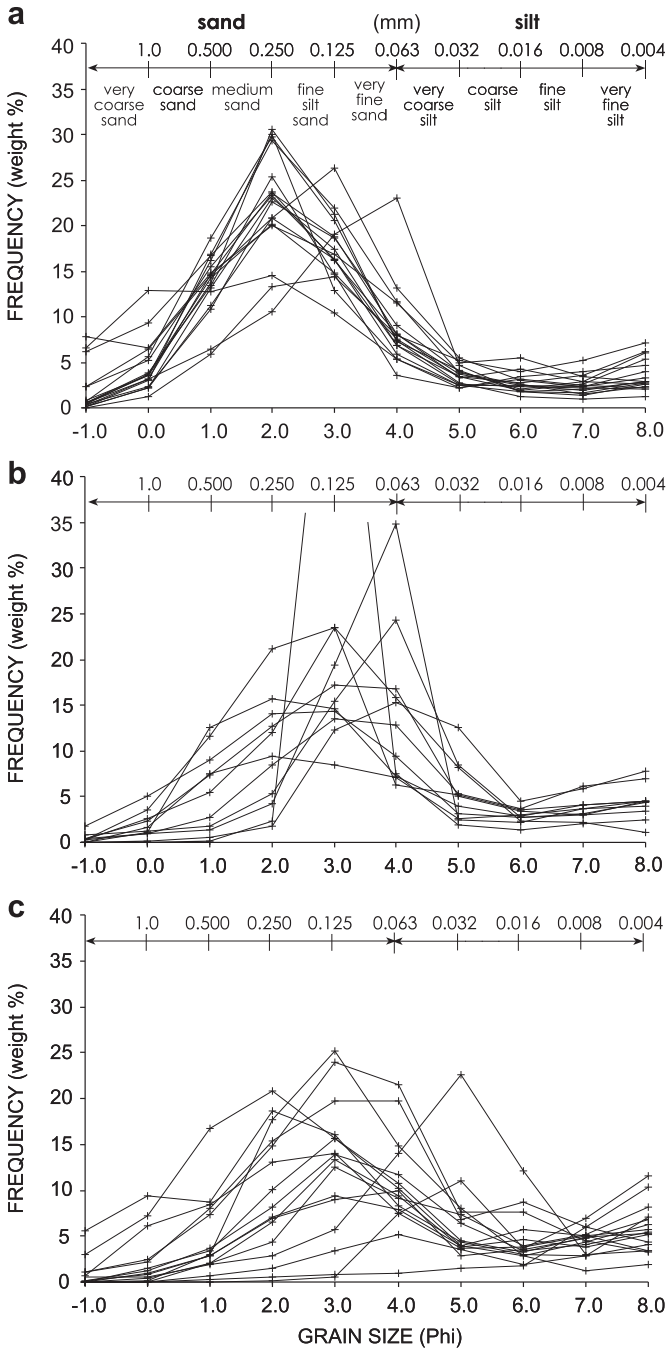

Fig. 7. (a) Grain size distributions of undeformed sandstones showing fine-skewed unimodal curves of poorly sorted, medium to fine sandstones. (b) Grain size distributions of footwall and hanging-wall damage zone sandstones showing the unimodal symmetrical curves of the poorly sorted, fine to very fine granular material. (c) Grain size distributions of fault core rocks. Curves are generally unimodal and symmetrical to slightly coarse skewed, with the exception of less deformed samples (i.e. sand blob and foliated sand).

fault zone evolution (Fig. 7b). The most abundant fractions in the analysed samples are the sand-size ones, which range from 30.09% to 75.77%, with a mean value of 51.1 ± 14.38% (Table A2 in the Appendix). The gravel-size fractions are strongly subordinate, ranging from 0% to 1.73%. The silt-size fractions range from 7.7% to 30.69%, with a mean value of 14.15 ± 2.17%. The residual clay-size fraction varies from 10.48% to 39.16% with a mean value of 32.8 ± 4.3%, higher than in the undeformed samples.

The modes of the damage zone samples, minus the residual clay-size fractions, range between Phi = 2 and Phi = 4. Mean grain diameters range from 3.10 to 5.98 with a mean value of 4.9 ± 0.66 (coarse silt). Sorting ranges between 2.4 and 3.33 with a mean value of 2.8 ± 0.33 (very poorly sorted). Skewness broadly ranges from −0.64 (coarse skewed curve) to 1.01 (fine-skewed curve), with a mean value of 0 ± 0.27 (symmetrical curve). Kurtosis varies between 1.33 (very platykurtic curve) and 3.34 (mesokurtic curve); the mean value is 1.7 ± 0.2 (platykurtic curve). Fractal dimensions are not homogeneous and vary from 2.62 to 3.65, with a mean value of 2.9 ± 0.17.

6.2. Porosity and permeability

A common result of dilatant structures in damage zones is that porosity is largely produced by pores with equivalent diameters >63 μm, reflected by the asymmetry of curves in Fig. 8d. Intergranular porosity is significantly higher than in the pristine sandstones, varying between 5.14 ± 0.6% and 9.07 ± 0.27%, with the exception of samples affected by intergranular extensional fractures that have porosities of about 2% (e.g. sample 12C-03) (Figs. 8b and 5d). Dilation bands formed in sandstones with mean porosity of about 4–6%; porosity within the dilation bands, however, is as high as 30%.

Permeability was measured in both footwall and hanging-wall damage zones of five fault zones (Fig. 8c). Permeability values span over three orders of magnitude, ranging from 7.61 md to 1033.95 md. Higher values were generally measured in the hanging-wall blocks (which, as mentioned above, typically exhibit better developed damage zones). The highest permeability values were recorded across localised dilation bands and extensional fractures, whereas the lowest ones were recorded across secondary fault splays. The mean permeability (the main Gaussian peak value) in the analysed damage zones varies from 26.83 ± 0.13 md to 172.81 ± 0.59 md.

7. Fault core characterisation

7.1. Grain size analysis

Grain size distribution curves of fault core samples are heterogeneous (Fig. 7c), showing differences even within the same fault core due to compositional and structural heterogeneities (e.g. Fig. 3b), as well as different displacement values that presumably caused different deformation intensities. Grain-size distribution curves are unimodal with the exception of two cases. The sedimentological characteristics of fault core samples are significantly different than the parent undeformed sandstones (Table A3 in the Appendix).

The most abundant grain-size fractions in 56% of the samples analysed are the silt- and residual clay-size ones. Exceptions are samples 5C-06 and 5D-06, which were taken from the stretched yellow sediment incorporated in the fault core and foliated sand, respectively; samples BR1A, B, and E, which are from a fault zone with displacement of ~7 m; and sample BR12A, where the sand size-fractions are most abundant. The amount of gravel-size material is quite small (0.78 ± 1.51%); sand-size fractions span from 2.59% to 70.51%, with a mean value of 34.4 ± 21.7%. The silt-size fractions range between 14.13% and 41.18%, with a mean value of 17.9 ± 1.4%. The clay-size fraction ranges from 5.71% to 77.92%, with a mean value of 41.3 ± 20.56%. The calculated mean grain size (Phi_m) of fault core rocks have a wide range of variability, from 2.85 (medium sand) up to 7.56 (very fine silt). The mean value is 5.5 ± 1.56. All samples are poorly (So = 1.22) to very poorly (So = 3.28) sorted with a mean value of 2.7 ± 0.31. Granulometric curves are generally symmetrical to very coarsely skewed, with the exception of sample 5C-06 and the samples taken from faults with

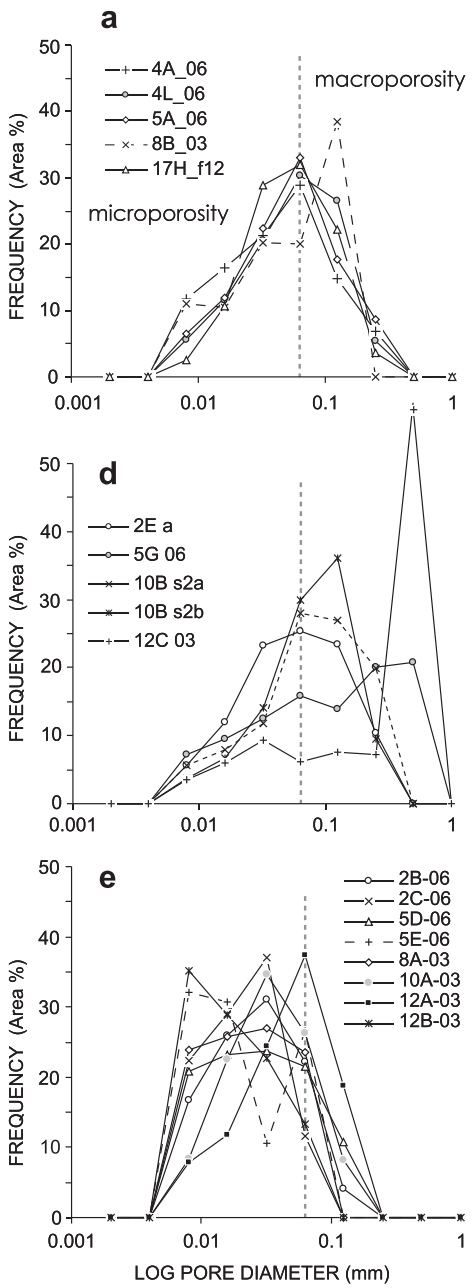

b

Sample	Poro (%)	St. dev.	Pores (n)	Image (n)	Displ. (m)
Undeformed					
4A-06	2.87	0.77	6122	4	-
4L-06	6.77	0.14	8582	4	-
5A-06	1.66	0.50	2270	4	-
BR8B	2.91	-	138	1	-
17H	3.43	1.25	3217	4	-
Damage zone					
2E-06	9.07	0.27	8194	3	20
5G-06	5.14	0.60	4342	2	14.5
10B a-03	7.30	0.35	1974	4	44.2
10B b-03	8.25	0.40	1825	2	44.2
12C-03	2.13	-	377	1	35
Fault core					
2B-06	2.25	0.70	5086	3	20
2C-06	0.19	0.09	367	2	20
5D-06	0.15	0.10	381	3	14.5
5E-06	0.16	0.11	383	2	14.5
8A-03	0.13	0.08	377	3	25.8
10A-03	0.46	-	240	1	44.2
12A-03	0.79	-	312	1	35
12B-03	0.13	-	342	1	35

c

Fault/ sample	Mean (md)	St. dev.	min (md)	max (md)	data (n)	Displ. (m)
Undeformed						
F10-03	4.33	0.53	0.63	48.8	17	-
F8-03	13.22	0.42	3.75	64	10	-
F5-03	2.86	0.15	2.04	90.1	6	-
F4-06	65.84	0.55	5	162.26	16	-
F5-06	70.35	0.26	37.61	233.69	11	-
F8-06	40.94	0.59	8.06	145.03	6	-
DB-06	2.61	0.35	0.68	93.4	35	-
Damage zone						
F2-06 F	32.88	0.53	7.61	95.2	9	20
F2-06 H	26.83	0.13	6.62	171.62	7	20
F4-06 F	95.73	0.27	20.34	659.96	20	12
F4-06 H	172.81	0.59	7.41	1531.46	15	12
F5-06 F	32.85	0.29	14.94	300.82	10	14.5
F5-06 H	82.52	0.63	23.41	1033.95	12	14.5
F8-06 F	82.35	0.2	8.52	192.01	14	49.6
F8-06 H	71.03	0.33	33.71	186.7	7	49.6
F12-3 H	112.71	0.3	16.25	346.13	38	35
Fault core						
F5-03	0.14	0.19	0.11	8.36	7	2.4
F10-03	4.35	0.34	0.6	48.4	48	44.2
F8-03	0.67	1.12	0.0039	27.4	13	25.8
F12-03	51.02	0.48	0.24	220	25	35
F2-06	22.18	0.31	6.26	62.5	7	20
F4-06	6.46	0.12	4.47	137.11	4	12
F5-06	15.8	0.56	3.19	35.66	7	14.5
F8-06	14.8	0.48	2.15	5263.82	21	49.6
DB-03	3.01	0.32	0.98	9.78	9	0.02

Fig. 8. Porosity and permeability data. (a) Pore area frequency distribution curves of the analysed images from undeformed samples. (b) Summary table showing the average porosity percentages in all the analysed samples. The number (*n*) of analysed pores and analysed images is indicated. Fault displacement values (Displ.) are also indicated. (c) Summary table showing results of Gaussian distribution statistics for permeability measurements in the undeformed, damage zone, and fault core rocks. All permeability values in the studied fault zones were measured in directions parallel to the fault strike. Mean values correspond to the main Gaussian peaks. (d) Pore area frequency distribution curves of the analysed images from damage zone samples, showing the relative abundance of macroporosity and microporosity. (e) Pore area frequency distribution curves of the analysed images from fault core samples, showing the relative abundance of microporosity and macroporosity.

displacement lower than 10 m. The shape of the granulometric curves ranges from very platykurtic to very leptokurtic, with a mean value of Ku = 2 ± 0.47. The fractal dimensions of the analysed samples range from 2.7 to 4.29; the mean value is 3.1 ± 0.2.

7.2. Porosity and permeability

In fault core rocks microporosity prevails with respect to macroporosity: very few large pores were found, whereas the bulk of pores show sizes generally lower than 63 μm (Figs. 6a,b and 8e). Total intergranular porosity in the analysed sections varies from 2.25 ± 0.7% to 0.13 ± 0.08% (Fig. 8b). Permeability was measured in fault core rocks of nine fault zones with different displacement values. Measurements were carried out in several sites within each fault core and their cumulative statistics are summarised in Fig. 8c. Permeability values are heterogeneous and span over 7 orders of magnitude from 0.0039 md to 5263 md. Statistical analysis indicates that the mean permeability of each fault core varies from 0.14 ± 0.19 md to 51.02 ± 0.48 md.

8. Particle shape analysis

The particle angularity data of undeformed, damaged and fault core sandstones from a fault zone with estimated displacement of

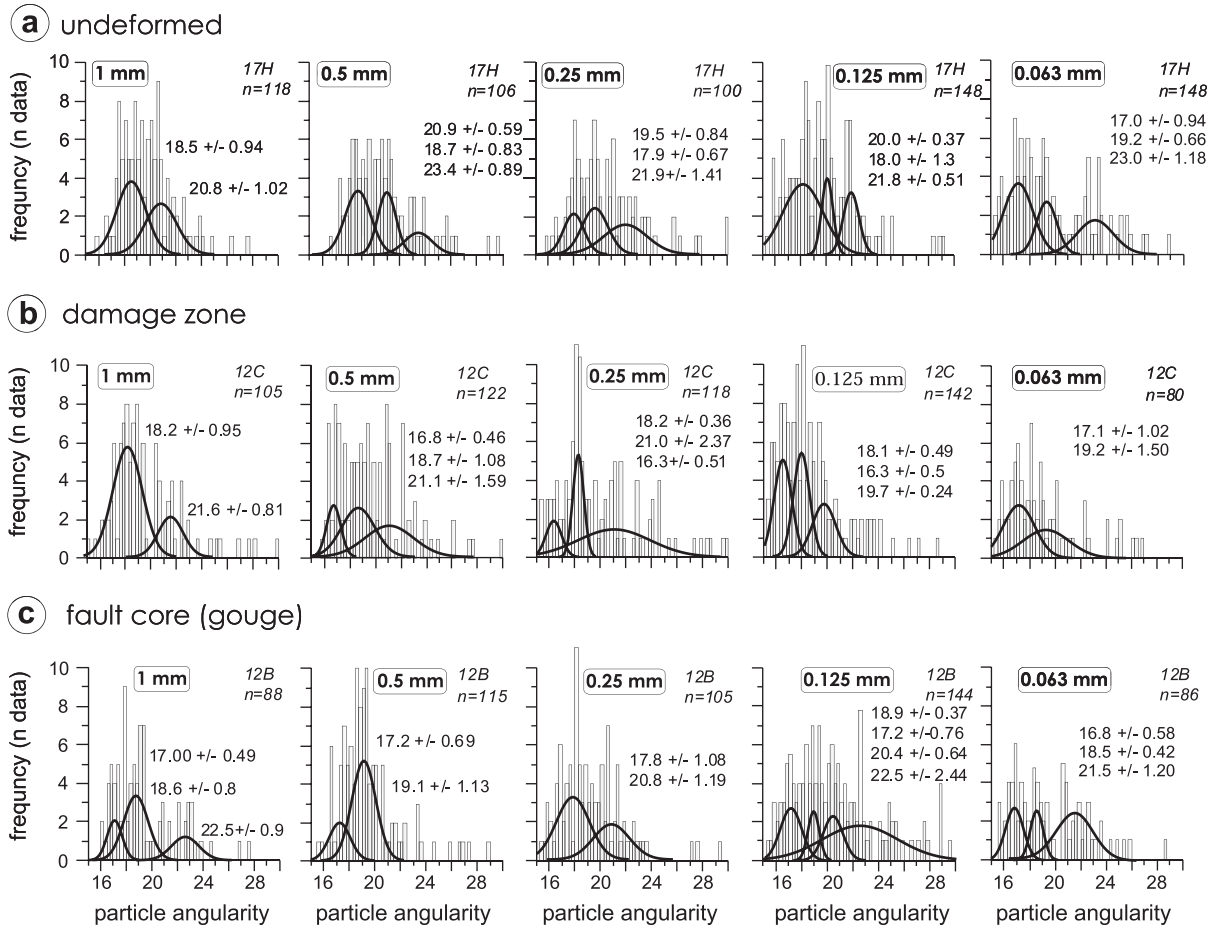

Fig. 9. Shape analyses of sand-size fractions showing the polymodal frequency distributions of grain angularity in the undeformed (a), damage zone (b), and fault core sandstones (c). Grain angularity plotted against frequency shows a polymodal frequency distribution in all analysed size classes. Best-fit Gaussian curves are superimposed on the corresponding data histograms. Sample name, Gaussian peaks, and related standard deviations, are also indicated.

~25 m are shown as frequency histograms (Fig. 9a–c) for the whole range of sand-size fractions (i.e. 1.0–0.063 mm). The angularity values obtained are extremely heterogeneous and broadly scattered between 15 (rounded particle) and 30 (very angular particle) in all the analysed size classes. Statistical data analysis shows the existence of polymodal distributions represented by Gaussian curves.

In the undeformed domain (Fig. 9a) the angularity of very coarse (1 mm) sand particles peaks at 18.5 ± 0.94, with a subordinate peak at 20.8 ± 1.02. Coarse undeformed sand particles (0.5 mm) have similar angularity with the main Gaussian peak at 18.7 ± 0.83, and two more angular peaks at 20.9 ± 0.59 and 23.4 ± 0.89. The main angularity of medium undeformed sand particles (0.25 mm) peaks at 19.5 ± 0.84, with two subordinate Gaussian peaks at 17.9 ± 0.67 and 21.9 ± 0.1.41. Angularity values of fine sand particles (0.125 mm) peaks at 18 ± 1.3, 20 ± 0.37 and 21.8 ± 0.51, respectively. Very fine sand particles (0.063 mm) have the lower angularity values which peaks at 17 ± 0.94, with two subordinate Gaussian peaks at 19.2 ± 0.66 and 23 ± 1.18.

In the damage zone (Fig. 9b), the main angularity of very coarse sand particles peaks at 18.2 ± 0.95, with a subordinated population at 21.6 ± 0.81. Coarse sand particles have peak angularity values of 18.7 ± 1.08, with two peaks at 16.8 ± 0.46 and 21.1 ± 1.59. Medium sand particle angularity is well clustered at 18.2 ± 0.36, with two peaks at 16.3 ± 0.51 and 21 ± 2.37. The angularity values of fine sand particles in the damage zone peaks at 18.1 ± 0.49, 16.3 ± 0.5 and 19.7 ± 0.24. The angularity of very fine sand particles is 17.1 ± 1.02, with a subordinate Gaussian peak at 19.2 ± 1.5.

Particle angularity in the fault core (Fig. 9c) is significantly different with respect to the previously described domains. Angularity of very coarse sand particles is 18.6 ± 0.8; a subordinate more rounded subpopulation shows at a mean value of 17 ± 0.49, while a third more angular subpopulation is 22.5 ± 0.9. Most coarse sand particles show angularity values averaged at 19.1 ± 1.13, with a subordinate rounded population at 17.2 ± 0.69. Angularity of medium sand particles peaks at 17.8 ± 1.8 and 20.8 ± 1.19, respectively. Fine sand particles are generally more angular and broadly scattered ranging from 22.5 ± 2.44 to 17.2 ± 0.76. The main angularity mode of very fine sand particles peaks at 21.5 ± 1.2, with two more rounded subpopulations showing means at 16.8 ± 0.58 and 18.5 ± 0.42, respectively.

9. Comparative analyses

9.1. Granulometric data

Cumulative grain size distributions representative of the undeformed, damage zone and fault core domains are compared in Fig. 10a. Data points defining each curve were obtained by averaging the corresponding frequency values for each Phi classes in the plots in Fig. 7. As expected, fault deformation produces a slight decrease in the mean grain size in the damage zones, especially in the secondary faults. In addition, the mean grain size is significantly reduced in the fault core rocks to a very fine silt-size material (Phi_m = 5.5 ± 1.56) (Fig. 10b). In particular, the sand-size content in the

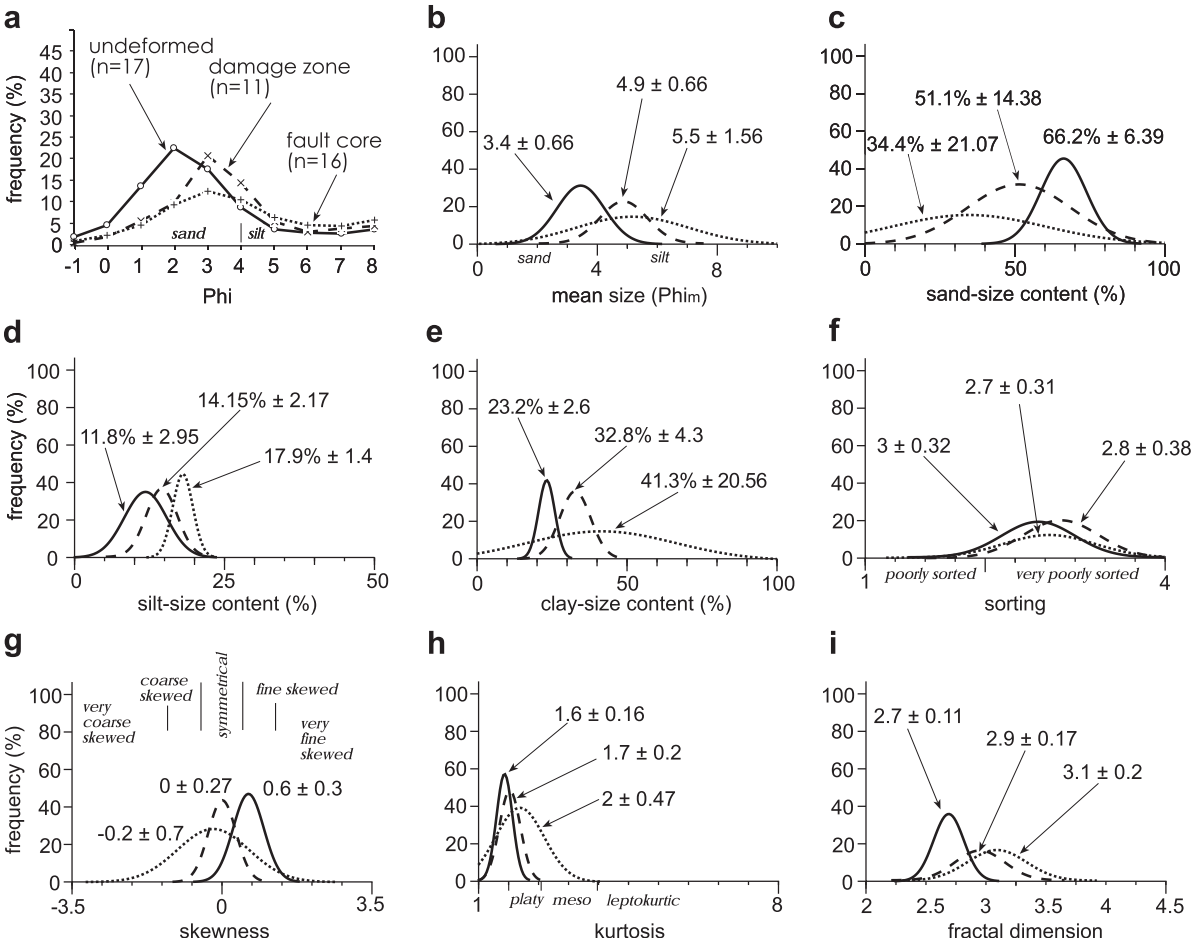

Fig. 10. Comparative granulometric data analyses of undeformed (solid line), damaged (dashed line) and fault core (dotted line) sandstones obtained by averaging the statistical parameters shown in Table A1, A2, and A3. (a) Grain size distributions curves, (b) mean grain size, (c) sand-size content, (d) silt-size content, (e) residual clay-size content, (f) sorting, (g) skewness, (h) kurtosis, (i) fractal dimension.

undeformed domain is significantly higher than in the damage zones and fault cores (Fig. 10c). These analyses therefore show a relative decrease in the sand-size fractions from undeformed to damage zone to fault core rocks and a corresponding increase in silt- and residual clay-size fractions (Fig. 10c–e). The latter reaches a mean value of about 41% in fault cores. Sorting, however, does not show significant variation across the three structural domains; all of the samples are very poorly sorted (So $>$ 2) (Fig. 10f), but undeformed sandstones are positively skewed toward the coarser sizes (Sk $>$ 0), whereas fault core samples display negative skewness towards the finer fractions (Sk $<$ 0) (Fig. 10g). Samples from damage zones show symmetrical grain size distributions (Sk $=$ 0). Mean kurtosis values show very platykurtic to platykurtic curves for all the three domains (Ku $<$ 2.55) (Fig. 10h). Samples from fault cores show higher values of kurtosis, indicating grain size distributions with a higher concentration around the mean size. The mean fractal dimensions systematically increase from the undeformed rocks ($D = 2.7 \pm 0.11$) to the damage zones ($D = 2.9 \pm 0.17$) to the more intensely deformed fault cores ($D = 3.1 \pm 0.2$) (Fig. 10i).

9.2. Porosity data

Microstructural analyses indicate that, in the 0.0088–1 mm pore size interval, porosity, pore size and pore size distribution are different in the three structural domains. Sandstones in undeformed domains have an average primary intergranular 2D porosity of about 3% (Fig. 11a), with large pores between sand- and silt-sized grains and a lot of micropores between finer particles. The ratio between macro and microporosity in undeformed sandstones is between 1 and 2 (Fig. 11b). Average porosity in damage zones is nearly three times of that of undeformed materials, even though not all samples show such an increase in bulk porosity (i.e. more compacted jointed samples) (Fig. 11a). The ratio between macro and microporosity is generally higher than in the undeformed sandstones, with values ranging between 1.4 and 4.4 (Fig. 11b).

Porosity and pore size in fault core samples are dramatically reduced with respect to both undeformed and damage zone rocks. In particular, average porosity in fault cores is about 6.6% of that in the undeformed ones, and about 2.3% of average porosity in damage zone rocks (Fig. 11a). Pores generally have dimensions less than 63 μm and thus the ratio between macro and microporosity is mostly lower than 1 (Fig. 11b).

9.3. Morphometric data

Undeformed sand grains are generally sub-angular to very angular: the main Gaussian peaks for all the size classes show angularity values (A) generally higher than 18, with the exception of very fine (<0.1 mm) sand particles, which are sub-rounded (Fig. 12a). The main Gaussian peaks (dark dots) show angularity between $A = 17$ and $A = 19.5$ which tends to decrease slightly with particle size. Particle angularity in the damage zone is not

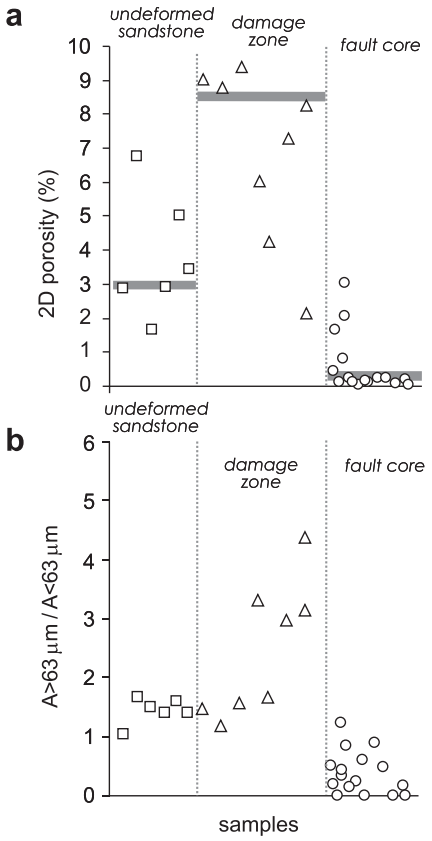

Fig. 11. Comparison of porosity (a) and macroporosity/microporosity ratio (b) among undeformed, damage zone and fault core sandstones, respectively. Dark grey lines indicate the average 2D porosity values in the undeformed (squares), damage zone (triangles), and fault core (circles) domains. A = pore area.

significantly different from respect to the undeformed sand fractions (Fig. 12b): particles are generally angular to very angular with main Gaussian peak values between $A = 17.1$ and $A = 18.7$. The only difference is the loss of the very angular ($A > 22$) subpopulations in the medium and finer sand size classes, which exhibit more rounded particles. Particle angularity is significantly different in the fault core, where angularity increases with decreasing particle size (Fig. 12c). Very coarse, coarse, and medium size sands in the core are mainly sub-rounded to sub-angular, ranging between $A = 17.2$ and $A = 18.6$; very angular coarser particles are almost completely absent and populations of newly formed rounded particles are common. In contrast, fine and very fine sand size fractions mainly consist of angular to very angular particles with a values higher than 21, even where relict sub-rounded populations derived from the undeformed sandstone are still present.

9.4. Permeability data

Measured permeability in undeformed sandstones ranges from about 10^{-1} to 10^{2} md, displaying two Gaussian peaks with mean Gaussian peak values of 2.52 ± 0.3 md and 43.68 ± 0.6 md, respectively. Best-fit unimodal Gaussian curve provides a mean value of 11.7 ± 0.9 md (Fig. 13a). Damage zone permeability is significantly higher, ranging over 4 orders of magnitude from about 10^{0} to 10^{3} md with a mean value of 86.9 ± 0.4 md (i.e., nearly eight times that of the undeformed sandstones) (Fig. 13b). Fault core permeability measurements taken from faults with different displacement span over six orders of magnitude, ranging from 10^{-2} to 10^{3} md. Cumulative statistics for the core measurements show a polymodal distribution with mean Gaussian peak values at 0.18 ± 0.3 md (~11% of data), 3.4 ± 0.3 md (~44% of data), 24.2 ± 0.3 md (~30% of data), and 87.5 ± 0.5 md (~15% of data). Best-fit unimodal Gaussian curve provides a mean value of 7.96 ± 0.7 md, about 68% of the undeformed sandstone mean permeability (Fig. 13c).

10. Across-fault data variability

Five fault zones were selected for horizontal transects across the fault strike. Each transect coordinate is centred on the master slip surface in the fault core. Samples and permeability measurements were collected in the same mechanical unit. Sample locations for grain size analyses are spaced every 40–80 cm, whereas permeability measurement points are spaced 20–50 cm apart in damage zones and 2–10 cm apart in fault cores.

10.1. Granulometric transects

Granulometric parameter variations along two representative transects are displayed in Fig. 14. All the statistical parameters change systematically across the fault zones, indicating changes in

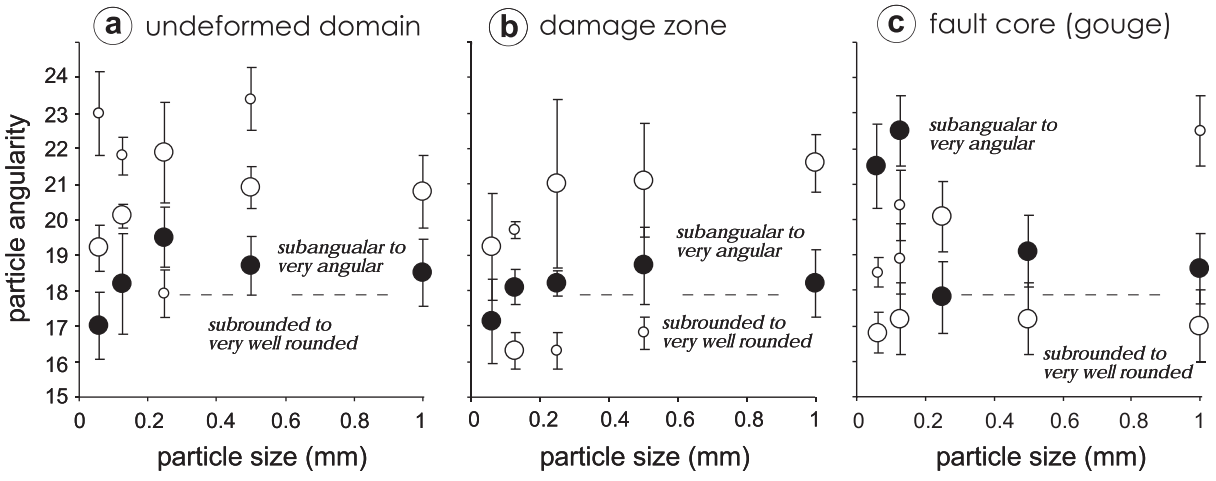

Fig. 12. Comparative shape analyses of undeformed (a), damage zone (b) and fault core (c) sand-size fractions, respectively. Larger black dots indicate the values of the largest Gaussian peaks, whereas larger clear dots indicate the values of the secondary Gaussian peaks. Smaller clear dots indicate the values of third- and fourth-order Gaussian peaks.

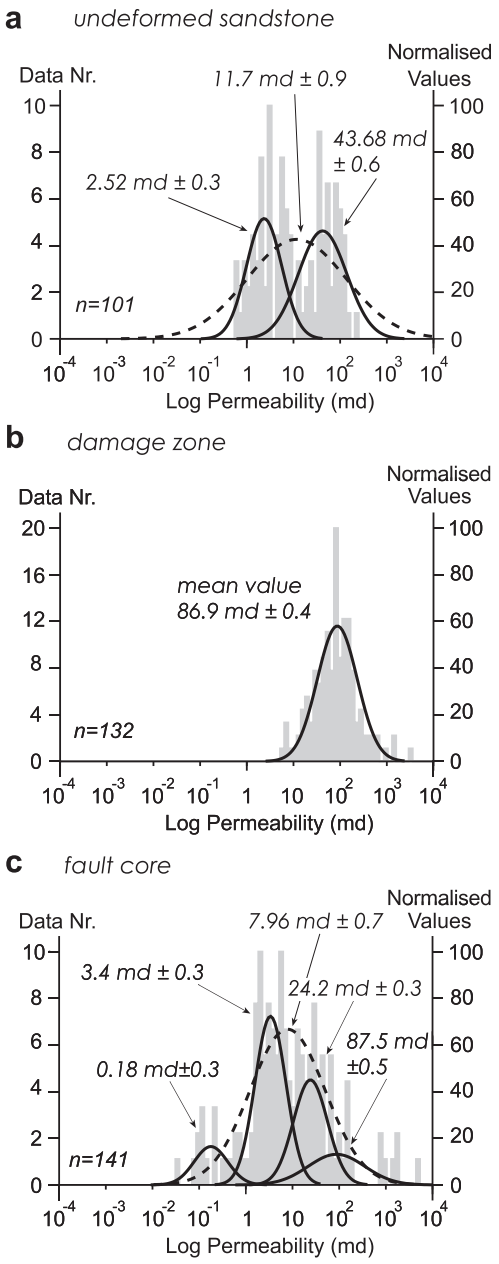

Fig. 13. Comparative permeability analyses of undeformed (a), damage zone (b) and fault core (c) sandstones, respectively. Best-fit unimodal Gaussian curves for undeformed and fault core permeability are indicated with a dotted line. Polymodal best-fit Gaussian curves are superimposed on the corresponding data histograms.

the shape of the corresponding granulometric curves, which are particularly dramatic in the fault cores. Mean grain size decreases (i.e., Phi_m increases) with deformation most dramatically in the fault core, where it sharply reaches the lowest values. Fine-skewed undeformed sandstones contrast with symmetrically skewed sandstones in the damage zones. Approaching the fault core, grain size distributions abruptly become strongly coarse skewed, indicating a significant increase in the finer grain size fractions (Fig. 14a and b). The very poor sorting of undeformed samples tends to improve slightly with deformation in damage zones, and strongly improves in the intensely deformed localised slip surfaces within the fault cores. Platykurtic undeformed samples change abruptly to meso to leptokurtic in the fault cores; no such significant modifications are evident in the damage zones (Fig. 14c and d). The percentage of residual clay-size fractions tends to increase locally in the damage zones (due to secondary fault spays) and abruptly increases in the fault cores, as much as to 70–80% for the most intensely sheared samples. Finally, the fractal dimension of about 2.7 in the undeformed sandstones gradually increases between 3 and 3.5 in the damage zones, then abruptly increases to values higher then 4 in the fault cores (Fig. 14e and f).

10.2. Permeability transects

Permeability measurements along five fault-perpendicular transects show values ranging between 10 and 100 md in the undeformed sandstones, and rather scattered and heterogeneous values in damage zones, that are mostly higher than in the adjacent undeformed sandstones and range between 10 and 1000 md (Fig. 15). Fault core permeability is typically reduced up to 1 order of magnitude from the average permeability of the host rock, although locally, the difference may be less or slightly more (compare values in Fig. 8c).

11. Fault displacement versus petrophysical properties in fault cores

11.1. Granulometric data

The ratio between mean grain sizes in fault cores and corresponding undeformed sandstones ($Phi_{m\ (core)}/Phi_{m\ (und)}$) generally increases with increasing displacement indicating a general decrease in the mean grain size in the faulted sandstones (Fig. 16a). The only exception is represented by the outlier at about 20 m of displacement, which is characterised by higher comminution intensity. Sorting tends to slightly deteriorate in two fault cores, while in the others it slightly improves with increasing displacement (Fig. 16b). Skewness ratios are generally negative and are not significantly influenced by fault displacement (Fig. 16c). On the other hand, the residual clay-size fraction ratios increase up to about 40 m of fault displacement, with the anomalously high value at about 20 m (Fig. 16d). Finally, the fractal dimension ratios ($D_{(core)}/D_{(und)}$) increase with increasing fault displacement, showing an outlier value at about 12 m of fault displacement (Fig. 16e).

11.2. Permeability

The fault core-undeformed sandstone ratios ($K_{(core)}/k_{(und)}$) are generally lower than 1, and irregularly decrease with increasing fault displacement, with the exception of a fault with a few centimetres of displacement that showed a slight increase in fault core permeability. Overall, they show an exponentially decreasing trend (Fig. 16f). As a first approximation, where fault zones accommodate displacements less than about 20 m, the average permeability reductions in the fault cores are of one order of magnitude. Where faults have displacements higher than about 20 m, the average permeability reductions locally reach two orders of magnitude, the only exception being an outlier (unfilled dot in the plot) that relates to an anomalously low permeability in the corresponding undeformed sandstones.

12. Discussion

12.1. Deformation mechanisms

Several lines of evidence indicate that deformation mechanisms in fault core and damage zone evolve from distributed to localised deformation during progressive sediment lithification.

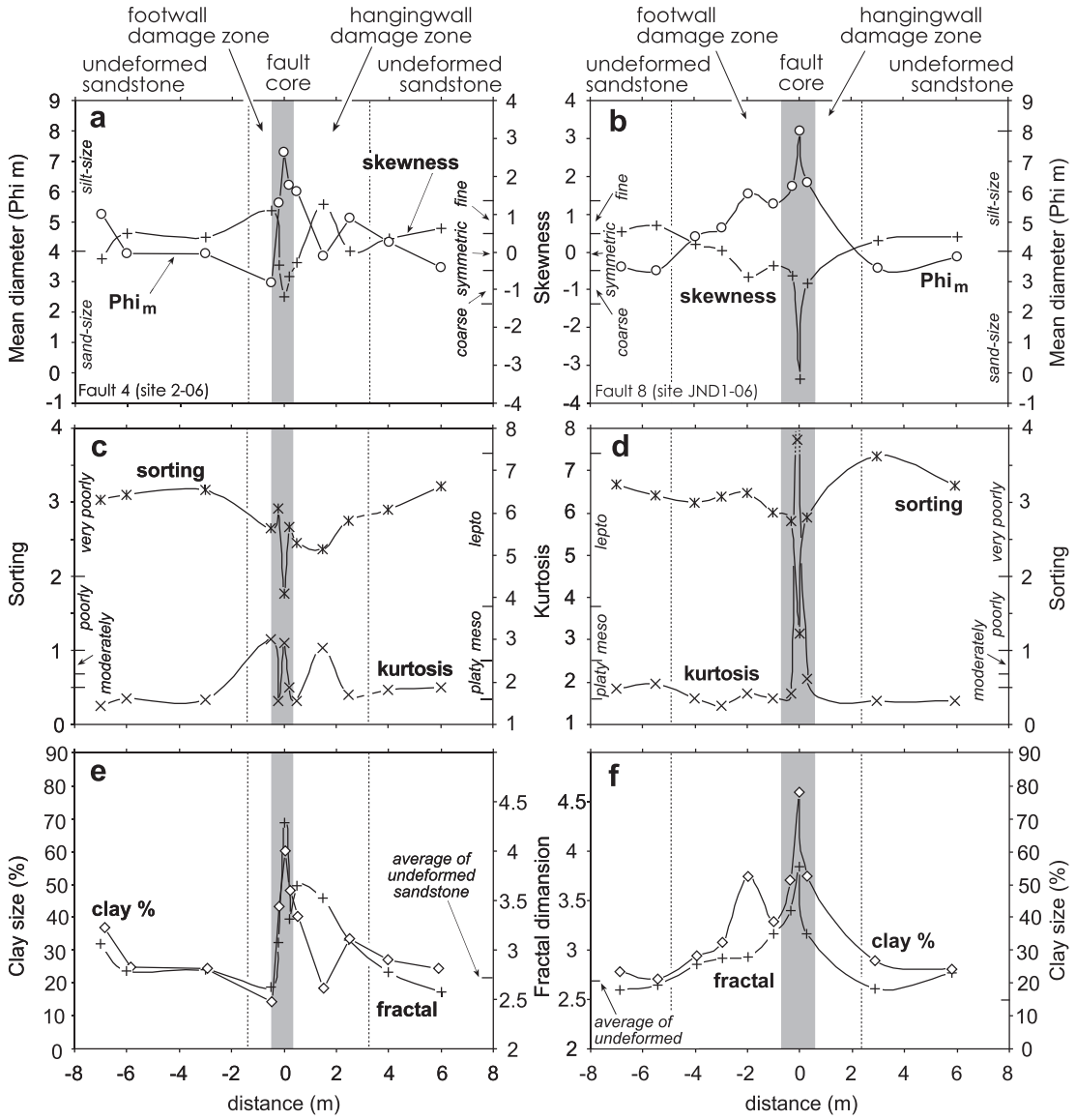

Fig. 14. Granulometric transects across two fault zones with displacements of about 12 m (Fault 4, left column) and 49 m (Fault 8, right column) illustrating the trends of mean size (Phi_m) and skewness (a, b), sorting and kurtosis (c, d), and clay-size content and fractal dimension (e, f), with increasing deformation. See text for details.

The loose packing fabric observed in thin section (Figs. 5c and 6d), the slight particle size (Fig. 10) and shape (Fig. 12a and b) variability, the relative abundance of sub-angular undamaged coarser grains (Figs. 5c and 6), and the higher porosity and asymmetric pore size distribution toward macropores (Fig. 8d), support deformation by non-destructive particulate flow of unlithified sediments (cf. Mandl et al., 1977; Maltman, 1994). In the fault core, this inference is supported by the macroscopically ductile distributed fabric (e.g. Rutter, 1986; Rawling and Goodwin, 2003) (Fig. 3). Effective fluid circulation is inferred to facilitate particle translation, rotation and grain boundary sliding with subordinated intragranular grain breakage (e.g. Sibson, 1977; Borradaile, 1981). Fluid-assisted environment is supported by the presence of elongate, foliated sand blobs with cuspate boundaries within the fault core (Fig. 3b and d) which are interpreted to represent an early incorporation of unlithified sand and sediment intermingling during fault slip. Non-destructive particulate flow is interpreted to occur in the early stages of the fault core evolution, whereas it persists throughout most of the damage zone history.

The progressive grain size reduction with increasing fault displacement (Fig. 16a) is interpreted to represent the progression from particulate flow with little cataclasis to localised cataclastic deformation in the fault core, particularly within the master slip surfaces (Fig. 14). Cataclastic deformation in fault core rocks is also confirmed by 1) the tight, matrix-supported foliated fabric (Fig. 6a and b); 2) intragranular fragmentation (Fig. 6c); 3) the reduction in porosity and pore size (Fig. 8c); 4) the occurrence of very angular finer grains surrounding coarser ones (Fig. 12c); and 5) the increase in clay-size fractions and fractal dimension compared to undeformed protoliths (cf. Sammis et al., 1987) (Fig. 16d and e). Compactional cataclastic flow is inferred to occur with progressive fragmentation of coarse grain at the impingement points (e.g. Gallagher et al., 1974) and chipping during rolling and translation, both rounding their initial angular shape and producing very angular small flakes. Elongate particles are generally reoriented into the sense of shear (cf. Goodwin and Tikoff, 2002). Similar results were found by previous workers in both rocks (e.g. Sammis et al., 1987; Blenkinsop, 1991; Storti et al., 2003) and poorly lithified sediments (cf. Heynekamp et al., 1999; Sigda et al., 1999; Cashman

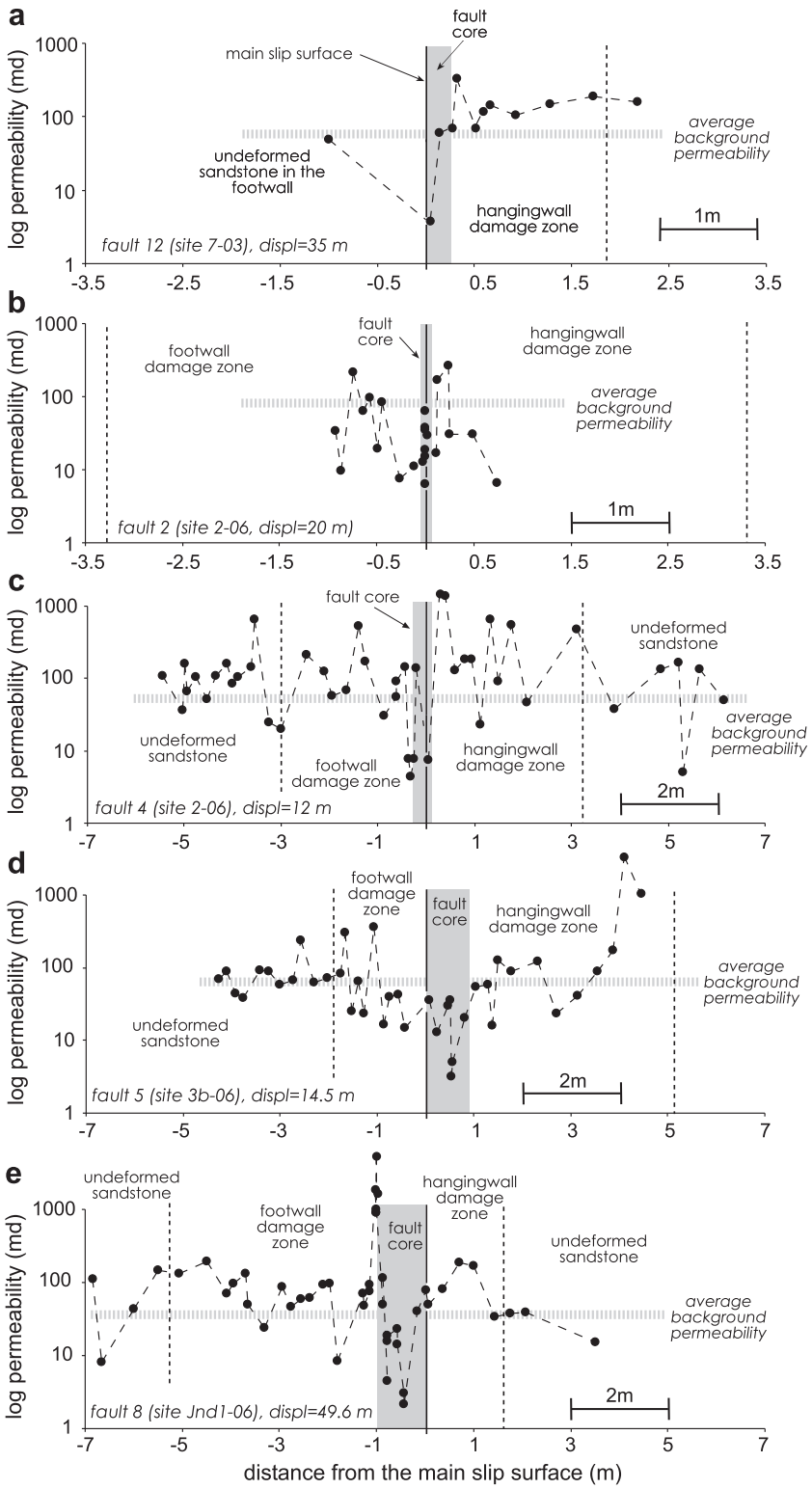

Fig. 15. Permeability transects across five fault zones with displacement of about 35 m (a), 20 m (b), 12 m (c) 15 m (d) and about 50 m (e). Permeability tends to be higher in the damage zones relative to undeformed sandstones, with the exception of secondary faults. Higher values were recorded across intergranular extensional fractures. In contrast, permeability is locally reduced more than one order of magnitude in fault core rocks.

and Cashman, 2000; Rawling and Goodwin, 2003, 2006; Cashman et al., 2007).

The non-linear trends of granulometric parameter ratios with respect to fault displacement (Fig. 16a–e) indicate that the fault rocks reach a level of grain size maturity beyond which few new grains are fractured, with the larger survivor grains presumably cushioned by the finer matrix material (e.g. Blenkinsop, 1991). Outliers may derive from non-uniformly distributed slip and compositional heterogeneities in fault cores. The change from distributed to localised cataclastic deformation in the fault core

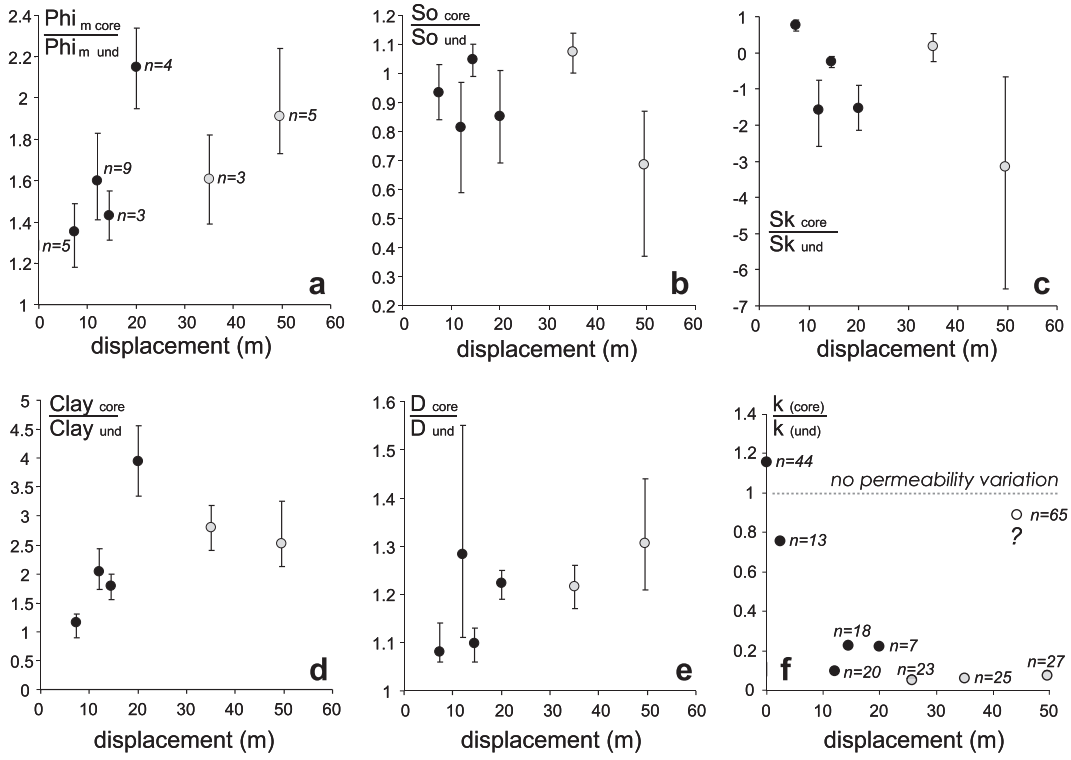

Fig. 16. Trends of the statistical granulometric parameters (a–e) and permeability reduction (f) in fault cores as a function of fault displacement. Each point in the graphs is given by the ratio between the mean value of a given parameter in the fault core and the mean value of the same parameter in the undeformed counterpart. Grey points relate to the fault zones which displacement values were inferred from the fault core thickness-displacement data in Fig. 4. Unfilled point in (f) represents a fault core where the mean permeability was similar to the anomalously, low permeable undeformed sandstone. Error bars represent the minimum and maximum values obtained from the corresponding end-member parameters. See text for details.

occurred during sediment lithification. This is confirmed by the presence of relatively rigid and internally undeformed sand pods (Fig. 3c) which supports an interpretation of tectonic entrainment and mixing of partially lithified sand units during late stage faulting (cf. Heynekamp et al., 1999; Rawling and Goodwin, 2006). A similar inference can be made for damage zones by the mutually overprinting relationships between intergranular extensional fracturing and Fe-oxide cementation in low-porosity sands (Fig. 5d–f), indicating progressive selective sediment strengthening during late stage faulting (cf. Caine and Minor, 2009).

The intergranular extensional fractures described in this study, developed by separation of the crack walls with jig-saw fit geometry along grain boundaries, can be considered a transitional failure mechanism between dilation bands of high-porosity sand(stone)s and transgranular extensional fractures of low-porosity, competent rocks.

12.2. Fault zone evolution

Field and laboratory analyses support a four-stage evolutionary model, where faulting of quartz-dominated granular material occurs during progressive Fe-oxide cementation under low confining pressure (Fig. 17). Nucleation of syn-sedimentary extensional shear zones in unlithified material slightly modifies the sedimentary fabric without significantly changing the pristine grain size distribution. At this stage, fault core and damage zone are not yet well defined and deformation results in dilational zones (Fig. 17a). Pore-size increase favours fluid drainage from undeformed sediments toward the shear zones, which can undergo transient overpressuring facilitating shear failure (Maltman, 1994). Fault zone architecture starts developing and shearing in the fault core is accommodated by particulate flow (cf. Borradaile, 1981; Rawling and Goodwin, 2003), possibly in a water-saturated environment (Fig. 17b). Grain breakage at this stage is negligible and distributed deformation in the damage zone is mostly achieved by dilatancy. This results in a general increase in bulk porosity and pore sizes that favour Fe-oxide cementation, likely occurring in a vadose environment as indicated by the patchily distribution of cement within the fault zone and meniscus cement in the undeformed sands (e.g. Lucia, 2007).

Incipient lithification promotes more localised, cataclastic deformation in the fault core (Fig. 17c) (cf. Lucas and Moore, 1986; Bernabe et al., 1992; Johansen et al., 2005; Rawling and Goodwin, 2006; Balsamo et al., 2008). Fault core thickness increases and porosity is reduced to less than 1%, favouring sealing behaviour. Widespread outcrop-scale folds develop and become disrupted during sediment mobilization (Maltman and Bolton, 2003) in the damage zone, facilitated to the loosening of the original interlocking of the densely packed sand grains. Non-destructive dilatant granular flow occurs in heterogeneous zones where fine-grained granular material is inferred to have moved into dilatant areas during deformation. As a result, porosity tends to increase by as much as 10%. Macroporosity exceeds microporosity due to the connection and growth of dilated pores.

As a consequence of progressive consolidation, deformation, cementation, and the increase of confining stress (cf. Engelder, 1974; Marone and Scholz, 1989), granular material strength

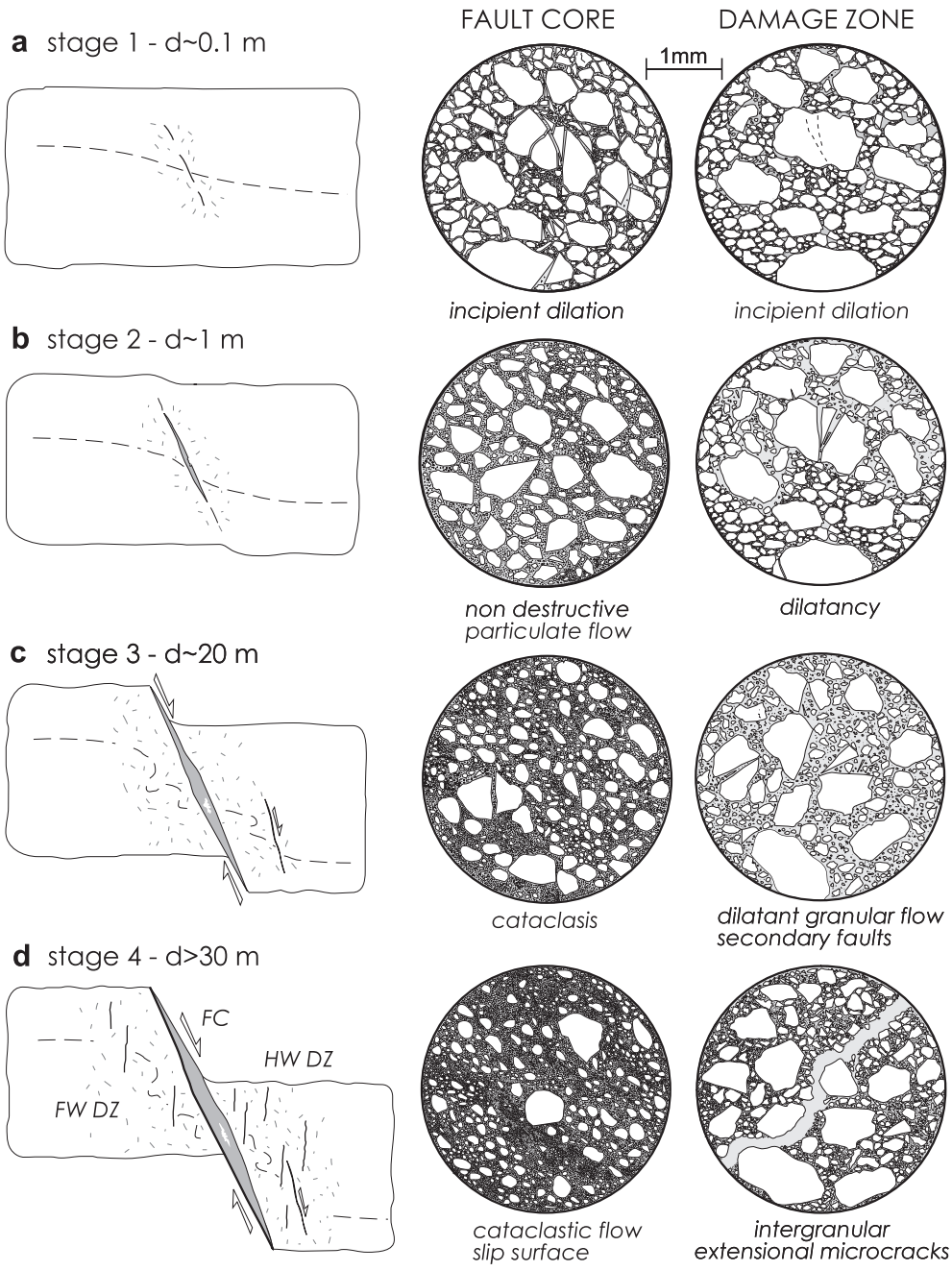

Fig. 17. Not to scale cartoon showing the proposed structural and hydraulic evolutionary model for extensional fault zones developed in low-porosity, quartz-dominated sand(stone)s during progressive lithification. Grain-scale deformation mechanisms inferred to have operated during fault zone evolution are indicated in circular magnified views of fault rocks. Images are drawn at the same scale. FC = fault core; FWDZ = footwall damage zone; HWDZ = hanging-wall damage zone; d = fault displacement. See text for details.

improves during deformation. Fault core and damage zone thicknesses continue increasing and incorporation of damage-zone material into the fault core produces overall grain-scale mixing which "feeds" the cataclastic process with new "undamaged" grains (Fig. 17d). Macroporosity is dramatically reduced by mechanical compaction and the production of finer particles during grain fracturing and abrasion. In the damage zone, non-destructive granular flow is inhibited by the resulting increase in sediment strength, and intergranular extensional fractures and dilation bands start to develop (Fig. 17d). Development of opening-mode structures results in an effective network of secondary fracture porosity (e.g. Laubach and Ward, 2006) which strongly increases macroporosity and secondary pore connectivity.

The time and space heterogeneous occurrence of dilatancy episodes and intergranular extensional fracturing in the damage zone are possibly favoured by transient fluid overpressuring pulses during fault history, which may be triggered by ineffective drainage during progressive burial (e.g. Maltman and Bolton, 2003), and by the improving hydraulic differentiation between low-permeable fault core and high permeable damage zone (e.g. Davis, 1999).

12.3. Fault zone hydraulic behaviour

The proposed evolutionary model implies that, when displacement is very low (< ~1 m), fault zones in low porosity, poorly lithified sediments are dominated by dilatant structures and, consequently, are expected to behave as preferential conduits for fluid flow (Fig. 17). As low porosity, low permeability fault core rocks develop, they provide increasingly efficient barriers to cross-fault fluid flow, and the hydraulic behaviour of fault zones progressively changes to conduit-barrier systems. In map view, fluid flow is enhanced along the fault strike of such systems, because the hanging-wall and footwall damage zones in which permeability is enhanced are separated by low permeability fault cores. Only fault tip regions may behave as outward migrating transient dilational conduits, for as long as the sandstones remain poorly cemented, such that particulate flow is possible.

Increasing fault displacement up to tens of meters during progressive sand lithification enhances the permeability contrast between fault cores and damage zones. In particular, fault cores suffer a strong permeability decrease by mechanical reduction of grain size, pore aperture size, and porosity as a result of cataclasis (e.g.; Pittman, 1981; Antonellini and Aydin, 1994; Sigda et al., 1999). Concomitant burial and cementation reduces primary porosity in damage zones. However, the related strength increase promotes the formation of localised dilatant structures, resulting in a further, more localised increase in sandstone permeability in the damage zones (Fig. 17).

The hydraulic behaviour described above is typical of low-porosity, well lithified rocks deforming by brittle fracturing (e.g. Caine et al., 1996; Storti et al., 2003), whereas poorly lithified (e.g. Rawling and Goodwin, 2003) and lithified high-porosity (e.g. Antonellini and Aydin, 1994; Shipton et al., 2002) sands and sandstones are typically considered to deform by deformation band faulting, and, in many cases, both damage zones and fault cores behave as hydraulic barriers, despite exceptions have been described (e.g. Fossen et al., 2007). The outcomes of this study show that high permeability damage zones are expected to form in poorly lithified sandstones that have low initial porosity, implying that faults in such rocks can channelize fluid flow. These observations could help to explain the existence of preferential fault-parallel flux in poorly lithified petroleum reservoirs (e.g. Silva et al., 2008). Moreover, the somewhat atypical hydraulic behaviour of the studied low-porosity sandstones confirms that initial porosity plays a fundamental role in determining the deformational structures form during fault zone evolution as proposed by Fossen et al. (2007) and, hence, fault zone hydrology. This is supported by the evidence that, for comparable displacement values, deformation in the studied fault cores caused an average permeability decrease of about two orders of magnitude, whereas in high-porosity sandstones the permeability reduction in fault cores is reported to reach at least four orders of magnitude (Antonellini et al., 1994; Sigda et al., 1999; Ogilvie and Glover, 2001; Shipton et al., 2002; Flodin et al., 2005).

13. Conclusions

The results of our structural, microstructural and petrophysical study of extensional fault zones in the continental Barreiras Formation are summarised as follows:

1) Deformation in faults formed in low-porosity, quartz-dominated, poorly lithified sandstones occurs initially by dilatant, non-destructive distributed particulate flow, which evolves with increasing slip and tectonic compaction to compactional cataclastic flow and deformation on localised slip surfaces. Angular original grains are progressively fragmented by transgranular fracturing and abraded as grain vertexes chip during grain rolling and translation. Rounded, coarse survivor grains are eventually cushioned by more angular, finer grained flakes in a tightly packed foliated rock. Progressive grain size reduction (to very fine silt) and the consequent increase in the silt- and clay-size fractions produce coarse-skewed granular material in which porosity (up to 0.2%) and average fault core rock permeability are reduced up to two orders of magnitude. Deformation in fault damage zones occurs initially by dilatant granular flow and secondary faulting, which do not significantly change grain size and shape distributions, but significantly alter grain packing. With increase sediment lithification, intergranular extensional fractures and dilation bands develop and result in an overall increase in porosity up to about 9% and pore connectivity, thereby increasing damage zone permeability. No deformation bands develop throughout the evolution of the studied fault zones.
2) Fault zones in low-porosity, poorly lithified sandstones produce hydraulic systems that evolve from conduits to barrier-conduit systems with progressive sandstone lithification and increasing slip. The permeability of fault cores decreases dramatically with slip up to ~20 m of fault displacement, after which it tends to decrease at a lower rate during further slip. This evolution in hydraulic behaviour is more similar to that of well lithified brittle rocks than that of deformation band-dominated, high-porosity sandstones.
3) The difference between fault core rock permeability and low-porosity, poorly lithified sandstone protoliths is generally less than that described for fault zones in high-porosity sandstones. This evidence further points to the crucial role of initial porosity and grain size properties (such as mean size and sorting) of host sandstones in predicting the structural evolution and hydraulic properties of fault zones in clastic material.
4) The documented trends between fault displacement and petrophysical properties (e.g., grain size distributions and permeability in fault core rocks), provide a useful tool for predicting grain size distribution, permeability, and transmissibility of subsurface fault zones in low-porosity, quartz-dominated sandstone fluid reservoirs. Our study shows that, given the enhanced porosity and permeability observed in the damage zones and the reduced porosity and permeability observed in fault cores, fault zone deformation in poorly lithified, low-porosity sandstones produce barrier-conduit systems, which can channelize flow parallel to faults, consistent with observations in some deep-water Brazilian clastic reservoirs.

Acknowledgements

This work was carried out under the framework of the *TRAFUR* and *TRAFUR2* (Transmissibility of Faults in Unconsolidated Rocks) research projects, funded by Petrobras, SA. We gratefully acknowledge Petrobras for releasing this material for publication. We are extremely grateful to Laurel Goodwin and Scott Minor for their constructive and helpful reviews that allowed us to significantly improve the final manuscript. Francisco Hilario Bezerra is kindly thanked for helpful discussion in the field. Josias Barreto is kindly thanked for logistic support in Icapuì. Isabela de Oliveira Carmo, Maria Lima and Paulo Vasconcelos are kindly thanked for discussions on age of Barreiras Formation.

Appendix

Table A1
Size-fraction frequencies and related grain size statistical parameters describing the mean size, sorting, skewness, kurtosis and fractal dimension of the analysed undeformed samples. R^2 is the coefficient of determination of the fractal dimension D, i.e. the square of the coefficient of correlation.

Sample	Gravel %	Sand %	Silt %	Clay %	Mean size Phi_m	Sorting So	Skewness Sk	Kurtosis Ku	Fractal D	R^2
2A-06	0.43	63.43	14.88	21.26	3.89	3.01	0.50	1.74	2.82	0.9671
2D-06	0.72	81.88	6.21	11.19	2.57	2.54	1.33	3.85	2.42	0.9711
4A-06	0.06	42.63	21.63	35.68	5.22	3.03	−0.19	1.43	3.06	0.9852
4B-06	0.10	62.73	13.36	23.81	3.93	3.10	0.48	1.62	2.79	0.9745
4C-06	0.47	60.47	15.83	23.23	3.95	3.16	0.38	1.58	2.80	0.9845
4D-06	0.57	76.26	10.24	12.94	2.98	2.65	1.09	3.02	2.63	0.9724
4L-06	0.50	62.25	11.31	25.94	4.31	2.90	0.36	1.82	2.77	0.9732
4M-06	2.37	66.07	8.14	23.43	3.46	3.22	0.61	1.87	2.57	0.9794
5A-06	0.25	68.27	11.11	20.37	3.54	2.98	0.70	2.01	2.68	0.9774
8A-06	2.29	65.01	9.17	23.53	3.51	3.23	0.55	1.84	2.59	0.9867
8B-06	0.85	67.98	9.94	21.23	3.41	3.10	0.72	1.96	2.65	0.9787
8J-06	6.61	55.97	10.58	26.84	3.49	3.62	0.33	1.54	2.61	0.9949
8L-06	0.61	60.81	14.30	24.28	3.87	3.22	0.43	1.56	2.77	0.9814
BR1C	6.10	73.90	12.98	7.01	2.34	2.63	0.93	3.22	2.61	0.9915
BR1D	7.75	69.81	16.76	5.67	2.50	2.60	0.69	2.94	2.71	0.9908
BR8B	0.08	73.70	14.73	11.49	3.31	2.52	0.94	2.83	2.79	0.9724
BR12D	0.10	82.75	10.22	6.94	2.64	2.25	1.35	4.21	2.63	0.9686
mean	1.76	66.2	11.8	23.2	3.47	3.00	0.60	1.60	2.70	0.98
st dev	2.53	6.39	2.95	2.6	0.66	0.32	0.30	0.16	0.11	0.01

Table A2
Size-fraction frequencies and related statistical parameters describing the mean size, sorting, skewness and kurtosis of the damage zone samples. The fractal dimension of the analysed samples is also indicated, as well as their structural position. (HW = hanging-wall damage zone; ms = mobilised sediments; sf = secondary fault; ext = intergranular extensional fractures). R^2 is the coefficient of determination of the fractal dimension D, i.e. the square of the coefficient of correlation.

Sample	Gravel %	Sand %	Silt %	Clay %	Mean size Phi_m	Sorting So	Skewness Sk	Kurtosis Ku	Fractal D	R^2	Structural position
2E 06	0.30	60.64	12.85	26.21	4.80	2.60	0.37	1.76	3.13	0.9632	HW-ms
4H-06	0.03	30.09	30.69	39.19	5.98	2.45	−0.29	1.54	3.65	0.9678	HW
4I-06	0.00	74.93	7.67	17.40	3.87	2.37	1.26	2.80	3.52	0.9158	HW
4J-06	0.84	48.03	18.74	32.40	5.13	2.75	0.02	1.71	3.10	0.9738	HW-sf
5F-06	1.73	51.84	13.28	33.15	4.53	3.33	0.02	1.46	2.78	0.9895	HW-ms
5G-06	0.00	51.03	15.48	33.49	4.70	3.20	0.06	1.33	2.93	0.9759	HW-ms
8C-06	0.43	56.32	14.89	28.36	4.50	2.99	0.21	1.61	2.86	0.9812	FW
8D-06	0.32	49.74	17.41	32.52	4.80	3.07	0.05	1.44	2.92	0.9855	FW
8E 06	0.00	34.12	13.31	52.57	5.92	3.13	−0.64	1.73	2.93	0.9884	FW
8F-06	0.34	38.57	22.26	38.82	5.59	2.86	−0.34	1.62	3.17	0.9844	FW
BR12C	0.25	75.55	13.72	10.48	3.10	2.40	1.01	3.34	2.62	0.9682	HW-ext
mean	0.39	51.10	14.15	32.8	4.90	2.80	0.00	1.70	2.90	0.97	
st dev	0.51	14.38	2.17	4.30	0.66	0.38	0.27	0.20	0.17	0.02	

Table A3
Size-fraction frequencies and related statistical parameters describing the mean size, sorting, skewness and kurtosis of the fault core samples. The fractal dimension of the analysed samples is also indicated, as well as their structural position within the fault core. R^2 is the coefficient of determination of the fractal dimension D, i.e. the square of the coefficient of correlation.

Sample	Gravel %	Sand %	Silt %	Clay %	Mean size Phi_m	Sorting So	Skewness Sk	Kurtosis Ku	Fractal D	R^2	Structural position
2B-06	0.00	10.67	15.35	73.98	7.56	1.92	−1.98	5.64	3.28	0.9898	Foliated sand
2C-06	0.02	28.35	17.43	54.20	6.32	2.81	−0.83	2.10	3.13	0.9879	Fault gouge
4E 06	0.15	38.58	19.36	41.92	5.60	2.92	−0.34	1.57	3.07	0.9844	Foliated sand
4F-06	0.00	8.15	33.14	58.71	7.28	1.77	−1.18	2.91	4.29	0.9801	Fault gouge
4G-06	0.02	28.54	24.58	46.86	6.18	2.66	−0.64	1.89	3.31	0.9839	Foliated sand
5C-06	5.61	61.15	14.15	19.09	3.35	3.23	0.45	1.93	2.70	0.9921	Sand blob
5D-06	0.70	49.16	18.24	31.89	4.65	3.28	−0.05	1.45	2.85	0.9944	Foliated sand
5E 06	0.00	41.38	17.82	40.80	5.48	2.97	−0.28	1.48	3.04	0.9848	Fault gouge
8G-06	0.00	31.23	17.51	51.26	6.19	2.75	−0.62	1.72	3.40	0.9584	Fault gouge
8H-06	0.00	2.59	19.49	77.92	8.01	1.22	−3.34	15.44	3.85	0.9946	Fault gouge
8I-06	0.12	29.45	17.92	52.51	6.29	2.80	−0.80	2.08	3.16	0.9865	Foliated sand
BR1A	1.14	70.00	23.15	5.71	3.37	2.21	0.62	3.09	2.92	0.9791	Foliated sand
BR1B	2.99	70.51	18.15	8.34	2.85	2.70	0.73	2.59	2.73	0.9922	Foliated sand
BR1E	1.10	65.06	25.93	7.91	3.61	2.41	0.49	2.55	2.97	0.9832	Foliated sand
BR12A	0.00	60.70	14.13	25.17	4.31	2.74	0.59	1.79	3.06	0.9252	Foliated sand
BR12B	0.59	24.85	41.18	33.38	5.65	2.41	−0.24	2.21	3.31	0.9739	Fault gouge
Average	0.78	34.40	17.90	41.30	5.50	2.70	−0.20	2.00	3.10	0.98	
St dev	1.51	21.07	1.40	20.56	1.56	0.31	0.70	0.47	0.20	0.02	

References

Anders, M.H., Wiltschko, D.V., 1994. Microfracturing, paleostress and the growth of faults. Journal of Structural Geology 16, 795–815.

Antonellini, M., Aydin, A., 1994. Effect of faulting on fluid flow in porous sandstones; petrophysical properties. American Association of Petroleum Geologists Bulletin 78, 355–377.

Antonellini, M.A., Aydin, A., Pollard, D.D., 1994. Microstructure of deformation bands in porous sandstones at Arches National Park, Utah. Journal of Structural Geology 16, 941–959.

Antonellini, M., Aydin, A., Orr, L., 1999. Outcrop-aided characterization of a faulted hydrocarbon reservoir: arroyo Grande Oil Field, California, USA. In: Haneberg, W.C., Mozley, P.S., Moore, J.C., Goodwin, L.B. (Eds.), Faults and Subsurface Fluid Flow in Shallow Crust. Geophysical Monograph, vol. 113. American Geophysical Union, pp. 7–26.

Aydin, A., 1978. Small faults formed as deformation bands in sandstone. Pure and Applied Geophysics 116, 913–930.

Aydin, A., 2000. Fractures, faults, and hydrocarbon entrapment, migration and flow. Marine and Petroleum Geology 17, 797–814.

Aydin, A., Johnson, A.M., 1978. Development of faults as zones of deformation bands and as slip surfaces in sandstone. Pure and Applied Geophysics 116, 931–942.

Balsamo, F., Storti, F., Piovano, B., Cifelli, F., Salvini, F., Lima, C.C., 2008. Time dependent structural architecture of subsidiary fracturing and stress pattern in the tip region of an extensional growth fault system, Tarquinia Basin, Italy. Tectonophysics 454, 54–69.

Bernabe, Y., Fryer, D.T., Hayes, J.A., 1992. The effect of cement on the strength of granular rocks. Geophysical Research Letters 19, 1511–1514.

Bezerra, H.F.R., Amaro, V.E., Vita-Finzi, C., Saadi, A., 2001. Pliocene-Quaternary fault control of sedimentation and coastal plain morphology in NE Brazil. Journal of South American Earth Science 14, 61–75.

Bezerra, H.F.R., Vita-Finzi, C., 2000. How active is a passive margin? Paleoseismicity in northeastern Brazil. Geology 28, 591–594.

Billi, A., Salvini, F., Storti, F., 2003. The damage zone-fault core transition in carbonate rocks: implications for fault growth, structure and permeability. Journal of Structural Geology 25, 1779–1794.

Blenkinsop, T.G., 1991. Cataclasis and processes of particle size reduction. Pure and Applied Geophysics 136, 59–86.

Borg, I., Friedman, M., Handin, J., Higgs, D.V., 1960. Experimental deformation of St. Peter Sand: a study of cataclastic flow. Geological Society of America Memoir 79, 133–191.

Borradaile, G.J., 1981. Particulate flow of rock and the formation of cleavage. Tectonophysics 72, 305–321.

Butler, B.C., Bell, J.D., 1989. Interpretation of Geological Maps, Longman Earth Science Series.

Caine, J.S., Evans, J.P., Forster, C.B., 1996. Fault zone architecture and permeability structure. Geology 24, 1025–1028.

Caine, J.S., Minor, S.A., 2009. Structural and geochemical characteristics of faulted sediments and inferences on the role of water in deformation, Rio Grande Rift, New Mexico. Geological Society of America Bulletin 121, 1325–1340.

Cashman, S., Cashman, K., 2000. Cataclasis and deformation-band formation in unconsolidated marine terrace sand, Humboldt County, California. Geology 28, 111–114.

Cashman, S.M., Baldwin, J.N., Cashman, K.V., Swanson, K., Crawford, R., 2007. Microstructures developed by coseismic and aseismic faulting in near-surface sediments, San Andreas fault, California. Geology 35, 611–614.

Chester, F., Evans, J., Biegel, R., 1993. Internal structure and weakening mechanisms of the San Andreas fault. Journal of Geophysical Research 98 (B1), 771–786.

Choquette, P.W., Lloyd, C.P., 1970. Geologic nomenclature and classification of porosity in sedimentary carbonates. American Association of Petroleum Geologists Bulletin 54, 207–244.

Davis, G.H., 1999. Structural geology of the Colorado plateau region of southern Utah, with special emphasis on deformation bands. Geological Society of America Special Papers 342, 1–157.

Du Bernard, X., Eichhubl, P., Aydin, A., 2002. Dilation bands: a new form of localized failure in granular media. Geophysical Research Letters 29 (24), 2176. doi:10.1029/2002GL015966.

Dunn, D.E., LaFountain, L., Jackson, R.E., 1973. Porosity dependence and mechanism of brittle fracture in sandstones. Journal of Geophysical Research 78, 2403–2417.

Engelder, J.T., 1974. Cataclasis and the generation of fault gouge. Geological Society of America Bulletin 85, 1515–1522.

Ferreira, J.M., Assumpção, M., 1983. Sismicidade no Nordeste do Brasil. Revista Brasileira de Geofisica 1, 67–88.

Ferreira, J.M., Oliveira, R.T., Takeya, M.K., Asssumpção, M., 1998. Superposition of local and regional stresses in northeast Brazil: evidence from focal mechanisms around the Potiguar marginal basin. Geophysical Journal International 134, 341–355.

Fisher, Q.J., Knipe, R.J., 2001. The permeability of faults within siliciclastic petroleum reservoirs of the North Sea and Norwegian Continental Shelf. Marine and Petroleum Geology 18, 1063–1081.

Flodin, E., Prasad, M., Aydin, A., 2003. Petrophysical constraints on deformation styles in Aztec sandstone, southern Nevada, USA. Pure and Applied Geophysics 160, 1589–1610.

Flodin, E.A., Gerdes, M., Aydin, A., Wiggins, W.D., 2005. Petrophysical properties of cataclastic fault rock in sandstone. In: Sorkhabi, R., Tsuji, Y. (Eds.), Faults, Fluid Flow, and Petroleum Traps. American Association of Petroleum Geologists Memoir, vol. 85, pp. 197–217.

Folk, R.L., Ward, W.C., 1957. Brazos river bar (Texas); a study in the significance of grain size parameters. Journal of Sedimentary Research 27, 3–26.

Fossen, H., Schultz, R., Shipton, K.Z., Mair, K., 2007. Deformation bands in sandstone – a review. Journal of the Geological Society 164, 755–769.

Fossen, H., Hesthammer, J., 1997. Geometric analysis and scaling relations of deformation bands in porous sandstone. Journal of Structural Geology 19, 1479–1493.

Fowles, J., Burley, S., 1994. Textural and permeability characteristics of faulted, high porosity sandstones. Marine and Petroleum Geology 11, 608–623.

Francus, P., 1998. An image-analysis technique to measure grain-size variation in thin sections of soft clastic sediments. Sedimentary Geology 121, 289–298.

Francus, P., Pirard, E., 2004. Testing for sources of errors in quantitative image analysis. In: Francus, P. (Ed.), Image Analysis, Sediments and Paleoenvironments, vol. 7. Kluwer Academic Publisher, pp. 87–102.

Gallagher, J.J., Friedman, M., Handin, J., Sowers, G.M., 1974. Experimental studies relating to microfracture in sandstone. Tectonophysics 21, 203–247.

Gibson, R.G., 1998. Physical character and fluid-flow properties of sandstone-derived fault zones. In: Coward, M.P., Johnson, H., Daltaban, T.S. (Eds.), Structural Geology in Reservoir Characterization. Geological Society of London, Special Publication, vol. 127, pp. 83–97.

Goodwin, L.B., Tikoff, B., 2002. Competency contrast, kinematics, and the development of foliations and lineations in the crust. Journal of Structural Geology 24, 1065–1085.

Griffiths, J.C., 1952. Grain-size distribution and reservoir–rock characteristics. American Association of Petroleum Geologists Bulletin 36, 205–229.

Haneberg, W.C., 1995. Steady-state groundwater flow across idealized faults. Water Resources Research 31, 1815–1820.

Heilbronner, R., Keulen, N., 2006. Grain size and grain shape analysis of fault rocks. Tectonophysics 427, 199–216.

Heynekamp, M.R., Goodwin, L.B., Mozley, P.S., Haneberg, W.C., 1999. Controls on fault-zone architecture in poorly lithified sediments, Rio Grande Rift, New Mexico: implications for fault-zone permeability and fluid flow. In: Haneberg, W.C., Mozley, P.S., Moore, J.C., Goodwin, L.B. (Eds.), Faults and Subsurface Fluid Flow in Shallow Crust. Geophysical Monograph, vol. 113. American Geophysical Union, pp. 27–49.

Inman, D.L., 1952. Measures for describing the size distribution of sediments. Journal of Sedimentary Research 22, 125–7145.

Johansen, T.E.S., Fossen, H., Kluge, R., 2005. The impact of syn-faulting porosity reduction on damage zone architecture in porous sandstone: an outcrop example from the Moab Fault, Utah. Journal of Structural Geology 27, 1469–1485.

Kim, Y.S., Peacock, D.C.P., Sanderson, D.J., 2004. Fault damage zones. Journal of Structural Geology 26, 503–517.

Krumbein, W.C., 1934. Size frequency distributions of sediments. Journal of Sedimentary Research 4, 65–77.

Krumbein, W.C., 1938. Size frequency distributions of sediments and the normal Phi curve. Journal of Sedimentary Research 3, 84–90.

Krumbein, W.C., 1941. Measurement and geological significance of shape and roundness of sedimentary particles. Journal of Sedimentary Research 11, 64–72.

Krumbein, W.C., Pettijohn, F.J., 1938. Manual of Sedimentary Petrography. Appleton-Century Company, New York.

Kwon, Q., Ngwenya, B.T., Main, I.G., Elphick, S.C., 2005. Permeability evolution during deformation of siliciclastic sandstones from Moab, Utah. In: Sorkhabi, R., Tsuji, Y. (Eds.), Faults, Fluid Flow, and Petroleum Traps. American Association of Petroleum Geologists Memoir, vol. 85, pp. 219–236.

Laubach, S.E., Ward, M.E., 2006. Diagenesis in porosity evolution of opening-mode fractures, middle Triassic to lower Jurassic La Boca Formation, NE Mexico. Tectonophysics 419, 75–97.

Lima, M., 2008. A história do Intemperismo na província Borborema Oriental, Nordeste do Brasil: implicações paleoclimáticas e tectônicas. 2008. PhD thesis, Universidade Federal do Rio Grande do Norte, Brazil.

Lucas, S.E., Moore, J.C., 1986. Cataclastic deformation in accretionary wedges. Deep Sea Drilling project Leg 166, southern Mexico, and on-land examples from Barbados and Kodiak Islands. In: Moore, J.C. (Ed.), Structural Fabrics in Deep Sea Drilling Project Cores from Forearcs. Geological Society of America Memoir, vol. 166, pp. 89–104.

Lucia, F.J., 2007. Carbonate Reservoir Characterization. An Integrated Approach. Springer, Berlin.

Mabesoone, J.M., Campos, E., Silva, A., Beurlen, K., 1972. Estratigrafia e origem do Grupo Barreiras em Pernambuco, Paraíba e Rio Grande do Norte. Revista Brasileira de Geociência 2, 173–190.

Mair, K., Main, I., Elphick, S., 2000. Sequential growth of deformation bands in the laboratory. Journal of Structural Geology 22, 25–42.

Maltman, A., 1994. Introduction and overview. In: Maltman, A.J. (Ed.), The Geological Deformation of Sediment. Chapman & Hall, London, pp. 1–35.

Maltman, A.J., Bolton, A., 2003. How sediments become mobilized. In: Geological Society of London Special Publications, vol. 216, pp. 9–20.

Mandl, G., de Jong, L.N.J., Maltha, A., 1977. Shear zones in granular material. Rock Mechanics and Rock Engineering 9, 95–144.

Manzocchi, T., Ringrose, P.S., Underhill, J.R., 2002. Flow through fault systems in high-porosity sandstones. In: Holdsworth, R.E., Turner, J.P. (Eds.), Extensional Tectonics: Faulting and Related Processes. The Geological Society of London, Key Issues in Earth Sciences, vol. 2, pp. 281–298. 2.

Marone, C., Scholz, C.H., 1989. Particle-size distribution and microstructures within simulated fault gouge. Journal of Structural Geology 11, 799–814.
de Matos, R.M.D., 1992. The northeast Brazilian rift system. Tectonics 11, 766–791.
McManus, J., 1988. Grain Size Determination and Interpretation. Techniques in Sedimentology. Backwell, Oxford.
Menéndez, B., Zhu, W., Wong, T.F., 1996. Micromechanics of brittle faulting and cataclastic flow in Berea sandstone. Journal of Structural Geology 18, 1–16.
Minor, S.A., Hudson, M.R., 2006. Regional survey of structural properties and cementation patterns of fault zones in the northern part of the Albuquerque basin, New Mexico – Implications for ground-water flow, U.S.G.S. Professional paper 1719.
Nelson, S.T., Mayo, A.L., Gilfillan, S., Dutson, S.J., Harris, R.A., Shipton, Z.K., Tingey, D.G., 2009. Enhanced fracture permeability and accompanying fluid flow in the footwall of a normal fault: the Hurricane fault at Pah Tempe hot springs, Washington County, Utah. Geological Society of America Bulletin 121, 236–246.
Ogilvie, S.R., Glover, P.W.J., 2001. The petrophysical properties of deformation bands in relation to their microstructures. Earth and Planetary Science Letters 193, 129–142.
Passchier, C.W., Trouw, R.A.J., 1996. Microtectonics. Springer, Berlin.
Pittman, D.E., 1981. Effect of fault-related granulation on porosity and permeability of quartz sandstones, Simpson Group (Ordovician), Oklahoma. American Association of Petroleum Geologists Bulletin 65, 2381–2387.
Rawling, G.C., Goodwin, L.B., Wilson, J.L., 2001. Internal architecture, permeability structure, and hydrologic significance of contrasting fault-zone types. Geology 29, 43–46.
Rawling, G.C., Goodwin, L.B., 2003. Cataclasis and particulate flow in faulted, poorly lithified sediments. Journal of Structural Geology 25, 317–331.
Rawling, G.C., Goodwin, L.B., 2006. Structural record of the mechanical evolution of mixed zones in faulted poorly lithified sediments, Rio Grande rift, New Mexico, USA. Journal of Structural Geology 28, 1623–1639.
Rotevatn, A., Fossen, H., Hesthammer, J., Aas, T.E., Howell, J.A., 2007. Are relay ramps conduits for fluid flow? Structural analysis of a relay ramp in Arches National Park, Utah. In: Geological Society, London Special Publications, vol. 270, pp. 55–71.
Rutter, E.H., 1986. On the nomenclature of mode of failure transitions in rocks. Tectonophysics 122, 381–387.
Storti, F., Billi, A., Salvini, F., 2003. Particle size distributions in natural carbonate fault rocks: insights for non-self-similar cataclasis. Earth and Planetary Science Letters 206, 173–186.
Salvini, F., 2004. Daisy 4.1 Software – The Structural Data Integrated System Analyzer. Available at. University of Roma Tre. http://host.uniroma3.it/progetti/fralab.
Sammis, C., King, G., Biegel, R., 1987. The kinematics of gouge deformation. Pure and Applied Geophysics 125, 777–812.
Selley, R.C., 2000. Applied Sedimentology. Academic Press, San Diego.
Shipton, Z.K., Cowie, P.A., 2001. Damage zone and slip-surface evolution over μm to km scales in high-porosity Navajo sandstone, Utah. Journal of Structural Geology 23, 1825–1844.
Shipton, Z.K., Evans, J.P., Robeson, K.R., Forster, C.B., Snelgrove, S., 2002. Structural heterogeneity and permeability in faulted Eolian Sandstone: implications for subsurface modeling of faults. American Association of Petroleum Geologists Bulletin 86, 863–883.
Sibson, R.H., 1977. Fault rocks and fault mechanisms. Journal of the Geological Society 133, 191–213.
Sigda, J.M., Goodwin, L.B., Mozley, P.S., Wilson, J.L., 1999. Permeability alteration in small-displacement faults in poorly lithified sediments: Rio Grande Rift, Central New Mexico. In: Haneberg, W.C., Mozley, P.S., Moore, J.C., Goodwin, L.B. (Eds.), Faults and Subsurface Fluid Flow in Shallow Crust. Geophysical Monograph, vol. 113. American Geophysical Union, pp. 51–68.
Silva, A.T., Lima, C.C., Faerstein, M., Salvini, F., Balsamo, F., 2008. Geomechanical model helps to explain unexpected high well productivity offshore Brazil. In: International Geological Congress, Oslo (abstract).
Suguio, K., Nogueira, A.C.R., 1999. Revisão crítica dos conhecimentos geológicos sobre a Formação (ouGrupo?) Barreiras do Neógeno e o seu possível significado como testemunho de alguns eventos geológicos mundiais. Geociências 18, 461–479.
Vernik, L., Bruno, M., Bovberg, C., 1993. Empirical relations between compressive strength and porosity of siliciclastic rocks. International Journal of Rock Mechancs and Mining Science 30, 677–680.
Walsh, J.J., Watterson, J., Heath, A., Gillespie, P.A., Childs, C., 1998. Assessment of the effects of sub-seismic faults on bulk permeabilities of reservoir sequences. In: Coward, M.P., Johnson, H., Daltaban, T.S. (Eds.), Structural Geology in Reservoir Characterization. Geological Society of London, Special Publication, vol. 127, pp. 99–114.
Walsh, J.J., Watterson, J., 1988. Analysis of the relationship between displacements and dimensions of faults. Journal of Structural Geology 10, 239–247.
Wise, D.U., Funiciello, R., Parotto, M., Salvini, F., 1985. Topographic lineament swarms: clues to their origin from domain analysis of Italy. Geological Society of America Bulletin 96, 952–967.
Wong, T., David, C., Zhu, W., 1997. The transition from brittle faulting to cataclastic flow in porous sandstones: mechanical deformation. Journal of Geophysical Research 102 (B2), 3009–3025.
Zhu, W., Wong, T., 1997. The transition from brittle faulting to cataclastic flow: permeability evolution. Journal of Geophysical Research 102 (B2), 3027–3041.